Additive Manufacturing 60 (2022) 103245

Contents lists available at ScienceDirect

Additive Manufacturing

journal homepage: www.elsevier.com/locate/addma

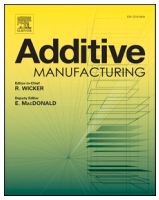

Review

The Trajectory of Additively Manufactured Titanium Alloys with Superior Mechanical Properties and Engineered Microstructures

Saeid Alipour [a], Atieh Moridi [b,*], Frank Liou [c], Arezoo Emdadi [a,*]

[a] Department of Materials Science and Engineering, Missouri University of Science and Technology, Rolla, MO 65409, USA
[b] Sibley School of Mechanical and Aerospace Engineering, Cornell University, Ithaca, NY 14853, USA
[c] Department of Mechanical Engineering, Missouri University of Science and Technology, Rolla, MO 65409, USA

ARTICLE INFO

Keywords:
Additive manufacturing
Titanium alloys
Engineered microstructure
Alpha prime
Alpha+Beta
Superior mechanical properties

ABSTRACT

Additive manufacturing (AM) plays a crucial role in the manufacturing and development of advanced materials including titanium alloys for engineering applications. During the last two decades, a great deal of effort has been devoted to print titanium parts with desired properties. However, due to presence of non-equilibrium/metastable phases, anisotropic microstructure, and various porosities in the printed titanium alloys, achieving an excellent combination of mechanical properties has been challenging. This review paper aims to provide a comprehensive overview of multiple post-process and in-process approaches to achieve enhanced strength-ductility combinations by microstructure engineering. Approaches such as addition of alloying elements/nucleants, multi-step post heat treatment, in-situ heat treatment, forced inter-pass cooling, in situ peening/rolling, hybridizing microstructure, high-intensity acoustic vibration, thermo-hydrogen refinement of microstructure, deliberately introducing lack of fusion defects with subsequent hot isostatic pressing are discussed in detail. Finally, we conclude by highlighting the challenges associated with each method and potential areas of improvement that can pave the way to develop reliable components with enhanced performance.

1. Introduction

Titanium (Ti) and its alloys are considered invaluable materials in aerospace, military, automotive and medical applications due to their superior properties such as high strength to weight ratio, high corrosion resistance and excellent biocompatibility [1–5]. Generally, based on their microstructure, Ti alloys are categorized into α (i.e., CP-Ti), α + compound (i.e., Ti-2.5% Cu), near α (i.e., Ti-8%Al-1%Mo-1%V and Ti-6%Al-2%Sn-4%Zr-2%Mo), α + β (i.e., Ti-6%Al-4%V and Ti-6%Al-2% Sn-4%Zr-6%Mo), metastable β (i.e., Ti-3%Al-8%V-6%Cr-4%Zr-4%Mo), and β (i.e., Ti-15%Mo-5%Zr-3%Al, Ti-15%Mo-%5Zr and Ti-15%Zr-4% Nb-4%Ta) alloys [6–11]. Among the various Ti alloys, Ti-6Al-4V alloy with exceptional mechanical, microstructural, and corrosion properties is considered one of the most widely used Ti alloys for various industrial [12,13] and medical applications [9,14,15].

Over the past few years, manufacturing Ti alloys (specifically Ti-6Al-4V) with tailored properties for specific applications has received considerable attention [16–18]. AM or three dimensional (3D) printing of Ti alloys in particular has made significant progress in the last two decades [19,20]. Achieving complex or porous geometries with unique properties and minimal material loss are some of the most significant advantages of AM compared to conventional manufacturing methods [9,21]. However, there are still some challenges that must be overcome to exploit the full potential of AM [22,23]. For instance, due to directional heat transfer and layer-by-layer production of printed parts, microstructures with columnar grains often form in printed samples after solidification. A columnar microstructure leads to anisotropic mechanical properties, particularly the ductility, and could limit the application of the manufactured part [23–26]. Besides, due to the difference between solidification conditions in X, Y, and Z directions, distribution of the grains along the different axes is not uniform [25]. Moreover, since the melt pool is very small and the movement of the heat source is quite fast, the typical microstructure mainly consists of non-equilibrium phases which could be either detrimental for mechanical properties or if designed properly, improve the performance of printed parts [24,27].

To address the aforementioned microstructural issues, various methods have been proposed [28,29]. One of the easiest and most widely employed solutions is the implementation of a post processing heat treatment [30–34] such as stress relief and annealing. This method will be described thoroughly in the conventional approaches section. Although the conventional heat treatment methods overcome the

* Corresponding authors.
E-mail addresses: moridi@cornell.edu (A. Moridi), emdadia@mst.edu (A. Emdadi).

https://doi.org/10.1016/j.addma.2022.103245
Received 10 August 2022; Received in revised form 7 October 2022; Accepted 19 October 2022
Available online 25 October 2022

Nomenclature

A	annealing.
AC	air cooling.
AFSD	additive friction stir deposition.
AM	additive manufacturing.
ASTM	American society for testing and materials.
CALPHAD	CALculation of PHAse Diagrams.
CCT	continuous cooling transformation.
CET	columnar to equiaxed transition.
CP-Ti	commercially pure titanium.
CNC	computerized numerical control.
DED	direct energy deposition.
DRX	dynamic recrystallization.
DSC	differential scanning calorimetry.
DZ	dead zone.
EBM	electron beam melting.
EBSD	electron backscatter diffraction.
El.	elongation.
FC	furnace cooling.
FSP	friction stir processing.
FSW	friction stir welding.
GTAW	gas tungsten arc welding.
HIP	hot isostatic pressing.
HSPT	hydrogen sintering and phase transformation.
HYTA	HYbridizing Titanium.
IPF	inverse pole figure.
IQ	image quality.
LAGB	low angle grain boundary.
LOF	lack of fusion.
LSP	laser shock peening.
M_s	martensite start.
M_f	martensite finish.
MCS	maximum compressive stress.
MHP	machine hammer peening.
MSHT	multi-step heat treatment.
OM	optical microscopy.
PDZ	plastic deformation zone.
PM	powder metallurgy.
PPDZ	partial plastic deformation zone.
REE	rare earth elements.
SEM	scanning electron microscopy.
SLM	selective laser melting.
SR	stress relieved.
STA	solution treatment and aging.
Ti	titanium.
TEM	transmission electron microscopy.
THRM	thermo-hydrogen refinement of microstructure.
Ti-5553	Ti-5 wt%Al-5 wt%V-5 wt%Mo-3 wt%Cr.
Ti-6Al-4 V	Ti-6 wt%Al-4 wt%V.
UTS	ultimate tensile strength.
WAAM	wire arc additive manufacturing.
ΔT_{fr}	freezing range.
3D	three dimensional.

formation of non-equilibrium microstructure and decomposition of martensitic phases to some extent, there are still challenges in achieving a completely uniform and equiaxed microstructure, eliminating the defects such as gas porosity and lack of fusion (LOF), as well as maintaining dimensional accuracy [35–37].

In addition to post processing heat treatment, other approaches have been recently developed to address the mentioned challenges either during or following the manufacturing process [37,38]. This study scrutinizes these state-of-the-art approaches including the addition of alloying elements/nucleants, in-situ heat treatment, high-intensity acoustic vibration, in-situ rolling, and deliberately introducing LOF with the subsequent hot isostatic pressing (HIP) to achieve printed Ti alloys with superior mechanical and microstructural properties.

This review paper focuses mostly on the microstructural evolution in the introduced techniques and its effect on mainly strength and ductility, with less emphasis on the other mechanical characteristics such as fatigue performance. There are a number of published review papers that comprehensively report the fatigue properties of the additively manufactured titanium alloys under various conditions such as as-built, stress-relieved, heat treated and hot isostatically pressed [39–44].

In Section 2, the conventional approaches to achieve strength-ductility synergy by microstructure engineering is discussed. In Section 3, state-of-the-art approaches are highlighted. First, each approach is presented, followed by an explanation of the machine setup or procedure and finally a description of the primary outcome. In Section 4, an Ashby plot summarizing the ultimate tensile strength versus elongation for different additive manufacturing approaches and the resultant microstructure is provided. This section is concluded by a discussion about the challenges or disadvantages that each method faces and an outlook to overcome the challenges.

2. Conventional approaches

A columnar microstructure due to directional heat transfer in AM, formation of voids (which are considered as a defect [45,46]) and the presence of non-equilibrium/metastable phases (i.e., α', α", and ω) due to the high cooling rates [47,48] are three major factors that control the mechanical properties of the printed products. Although the formation of small voids and porosities might be reduced by adjusting the processing parameters [49–52], in some cases a post processing treatment is required to achieve a tailored microstructure [53–55].

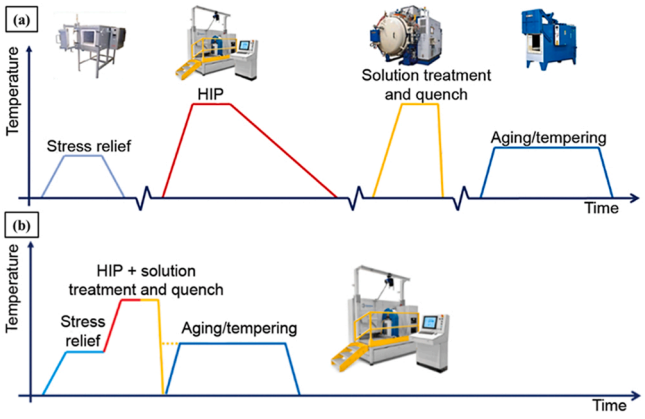

Fig. 1. (a) The schematic of different conventional thermal post-processing for printed parts (stress relief, HIP, solution treatment and quench, aging/tempering), (b) an example of combined post-processing treatment for a printed part (stress relief+HIP+solution treatment and quench+aging/tempering). Figure reproduced from [56].

Fig. 1(a) depicts a schematic of conventional thermal post-processing methods for improving the microstructure and mechanical properties of printed parts [56] including the stress relief process [57,58], HIP process [59,60], solution treatment and quench [61–63], and aging/tempering [64,65]. Additionally, there are some hybrid approaches which include two or more of the previous thermal post-processing methods. For

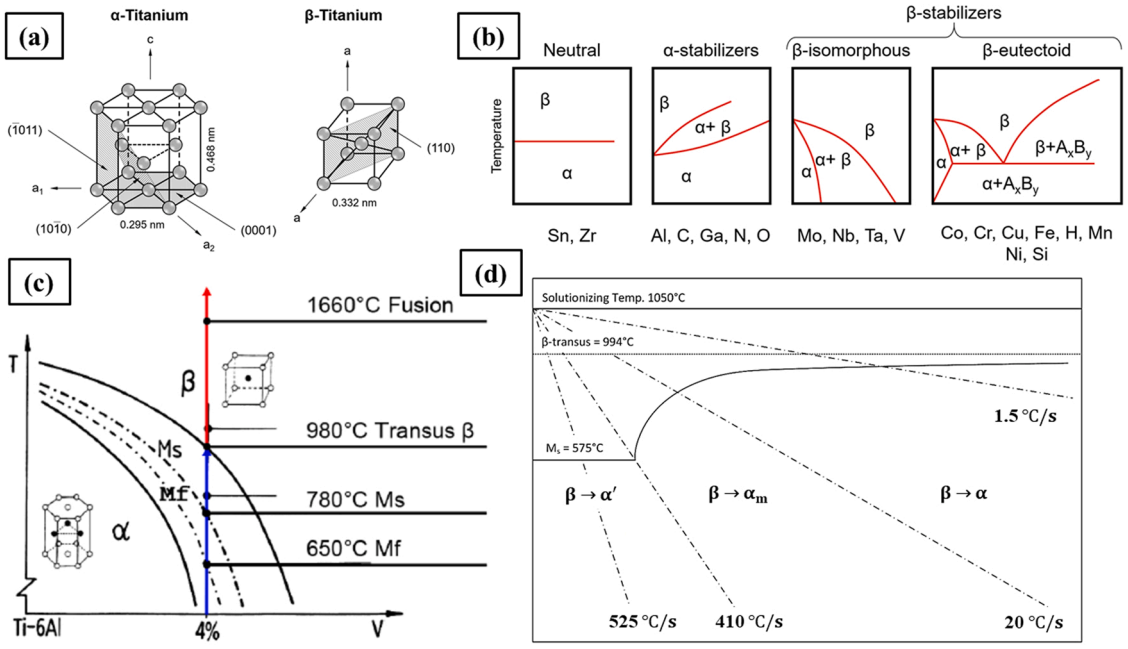

Fig. 2. (a) A schematic of the α and β crystal structure, b) the effect of different alloying elements (i.e., α-stabilizer, β-stabilizer, or neutral element) on the equilibrium phase diagram of Ti alloys [74], (c) diagram of temperature versus V wt% of Ti-6Al alloy with stable phases at different temperatures for Ti-6Al-4V alloy [77], (d) CCT diagram for Ti-6Al-4V alloy to show the effect of cooling rate on phase transformations [78].
Figures reproduced from [74,77,78].

example, in Fig. 1(b) a four-step treatment including stress relief, HIP, solution treatment and quench, as well as aging/tempering is conducted to relieve stresses and subsequently to modify the microstructure [56]. In the following sections, these conventional methods are presented in detail.

2.1. Post-heat treatment processes

One of the earliest and simplest techniques to address the challenges in microstructure and consequently in the mechanical properties of Ti alloys is to perform a heat treatment process after manufacturing

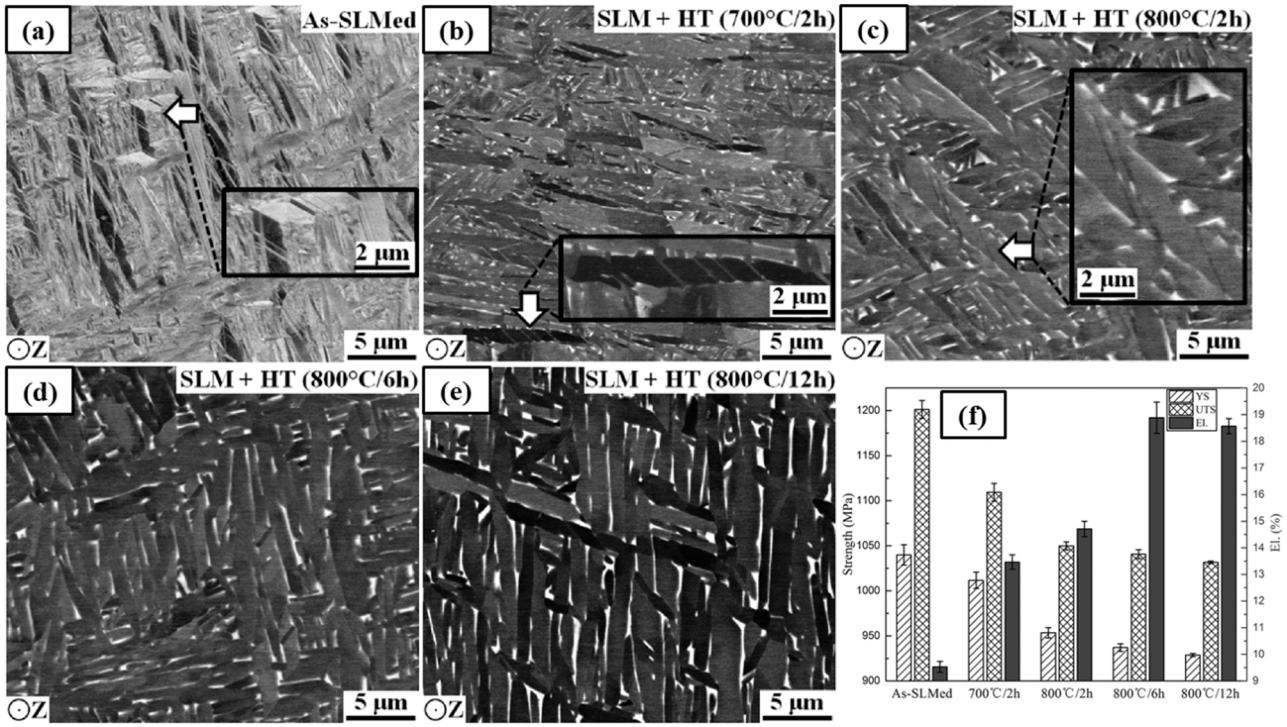

Fig. 3. Scanning electron microscopy (SEM) images of (a) SLM without any heat treatment, (b) SLM and heat treated at 700 ℃ for 2 h, (c) SLM and heat treated at 800 ℃ for 2 h, (d) SLM and heat treated at 800 ℃ for 6 h, and (e) SLM and heat treated at 800 ℃ for 12 h, (f) yield strength, ultimate tensile strength, and elongation of these samples.
Figure reproduced from [79].

Table 1
A summary on the successful A and STA heat treatment of additively manufactured Ti-6Al-4V to achieve excellent mechanical properties.

Manufacturing Method	A or STA Temperature	A or STA Time & Cooling Condition	Final Microstructure	Mechanical Properties	Ref.
SLM	A (800 °C)	A (6 h+FC)	α + β	UTS: 1041 MPa El.: 18.9%	[79]
DED	STA (950 °C+540 °C)	STA (1 h+AC+4 h+AC)	α + β	UTS: 1206 MPa El.: 13.42%	[81]
DED	A (760 °C)	A (1 h+AC)	α + β	UTS: 1044 MPa El.: 10%	[82]
SLM	A (850 °C)	A (2 h+FC)	α + β	UTS: 1004 MPa El.: 12.84%	[83]
SLM	A (1020 °C)	A (1 h+FC)	α + β	UTS: 833 MPa El.: 14.5%	[84]
SLM	A (730 °C)	A (2 h+FC)	α + β	UTS: 1057 MPa El.: 12.4%	[50]
EBM	STA (925 °C+450 °C)	STA (1 h+AC+4 h+AC)	α + β	UTS: 1090 MPa El.: 15.5%	[80]
EBM	STA (1050 °C+500 °C)	STA (2 h+AC+10 h+AC)	α + β	UTS: 978 MPa El.: 16.5%	[85]

[66–68]. Several studies have shown that applying a heat treatment above the beta transus temperature (approximately 1000 °C) can transform the microstructure of printed Ti-6Al-4V from columnar to equiaxed grains [63,69]. Hence, annealing (A) and solution treatment and aging (STA) are considered as the conventional heat treatment processes [70–72]. Recently, new heat treatment approaches, such as multi-step heat treatment (MSHT) and innovatively designed globularization heat treatment, have been developed to produce Ti alloys with improved mechanical properties [71–73]. To eliminate the need for plastic deformation before the heat treatment in gloularization, repeated thermal cycling close but below the β transus temperature is performed to form globular α grains [71].

Fig. 2(a, b) depicts a schematic of the α and β crystal structures and the effect of different alloying elements on Ti phase diagrams. Alloying elements such as Al, C, N, and O are α-stabilizers while Mo, Nb, Ta, and V are isomorphous β-stabilizers. In addition, some other alloying elements such as Co, Cr, Cu, Fr, Ni, Mn, Si, and H are eutectoid β-stabilizers. On the other hand, having elements such as Zr and Sn does not change the microstructure and they are considered as neutral alloying elements [12, 74]. Fig. 2(c) shows a schematic of the pseudo-binary phase diagram of the Ti-6Al-4V alloy as the most well-known Ti alloy. As illustrated in Fig. 2(c), by increasing the temperature, the alloy with 4 wt% V enters the α+β dual phase region. Between 780 °C and 980 °C, it is expected that the α' phase (which is formed due to the high cooling rates) transforms into the dual phase α + β microstructure after annealing with subsequent aging heat treatment. However, the martensitic decomposition temperature is not always constant; it depends on the manufacturing method and primary microstructure of Ti-6Al-4V alloy. In a study conducted by Sallica-Leva et al. [67] α' decomposition temperature was measured for SLMed porous Ti-6Al-4V through differential scanning calorimetry (DSC) method. Their results indicated that α' decomposition occurs between 760 °C and 850 °C, which differs from the range mentioned earlier. In general, experimental results revealed superb elongation for heat treated Ti-6Al-4V alloy with α + β dual phase microstructure compared to as-printed Ti-6Al-4V with non-equilibrium/metastable phases [74,75]. The final microstructure is controlled by the temperature of the heat treatment as well as the cooling rates [76]. As indicated by the micrographs in Fig. 2(d), if the cooling rate is faster than 410 °C/s, the final microstructure will be mostly an α' phase. However, if the cooling rate is kept below 20 °C/s, the α' phase will no longer form and the microstructure will include the α phase.

In a study conducted by Cao et al. [79], the microstructure and mechanical properties of Ti-6Al-4V alloy manufactured by the SLM method were investigated. Printed specimens were subjected to annealing heat treatment at different temperatures and the results were compared to non-heat treatment (as-built) specimens.

Fig. 3(a-f) shows Ti-6Al-4V microstructures before and after annealing heat treatment as well as their tensile results, respectively. The results of this study revealed that by applying annealing heat treatment at minimum 800 °C for 6 h and 12 h with subsequent furnace cooling, the α' phase, which was created due to rapid solidification, transformed into a dual phase α + β and caused relatively high ultimate tensile strength (UTS) of 1041 MPa and excellent elongation of 18.9%. This study showed that at temperatures lower than 800 °C, the martensite could not fully transform to other phases and resulted in smaller strain to failure.

Several studies have explored the effect of cooling rate after heat treatment near beta transus temperature on the resulting microstructure of printed Ti-6Al-4V [61,80]. Muhammad et al. [61] investigated the effect of heat treatment at 950 °C for 1 h followed by separate cooling in water (water-quenched), air (air-cooled), or furnace (furnace-cooled), respectively. For the highest cooling rate, which is water quenching, the martensitic α' is formed in prior β grains with needle-like microstructure. However, after intermediate cooling rates, i.e., when the samples were air-cooled, a modified β structure formed by secondary α laths precipitating in the matrix. Due to a low to moderate rate of cooling in furnace-cooled, α-lamellae are formed by diffusion-controlled nucleation and growth of α platelets into β grains.

Table 1 summarizes other available literature on A and STA post processing heat treatments of printed Ti alloys to achieve improved mechanical properties.

MSHT is one of the recent techniques that was proposed based on a series of heat treatments at different temperatures below the transus temperature (~ 990°C) to decompose and globalize the α′ martensitic microstructure and generate nearly equiaxed microstructure [71].

Fig. 4(a) shows the sequence of the different times and temperatures applied to the SLM Ti-6Al-4V samples. The samples were subjected to consecutive 950, 850, 750, 650 °C temperatures and remained at those temperatures for 2 h and then cooled inside the furnace to room temperature.

Fig. 4(c-f) illustrate the microstructural evolution at each step of the heat treatment respectively. The authors showed that the martensitic α′ phase is transformed to α+β microstructure, and equiaxed α grains are found at three different positions which are the original columnar boundary, plate α, and fine α grains. As can be observed, lowering the temperature from 950° to 650°C reduces the β volume fraction from 26.5% to 6.4%. This can result in a small number of low angle grain boundaries (LAGBs) emerging in the α lamellae which can facilitate globularization during subsequent thermal activation.

Fig. 4(b) illustrates the tensile properties of MSHTed samples and other conventional heat treatment methods for Ti-6Al-4V alloy. The MSHTed Ti-6Al-4V sample exhibited an excellent ductility of 21.8% with a moderate UTS of 953 MPa which proves that a wide range of

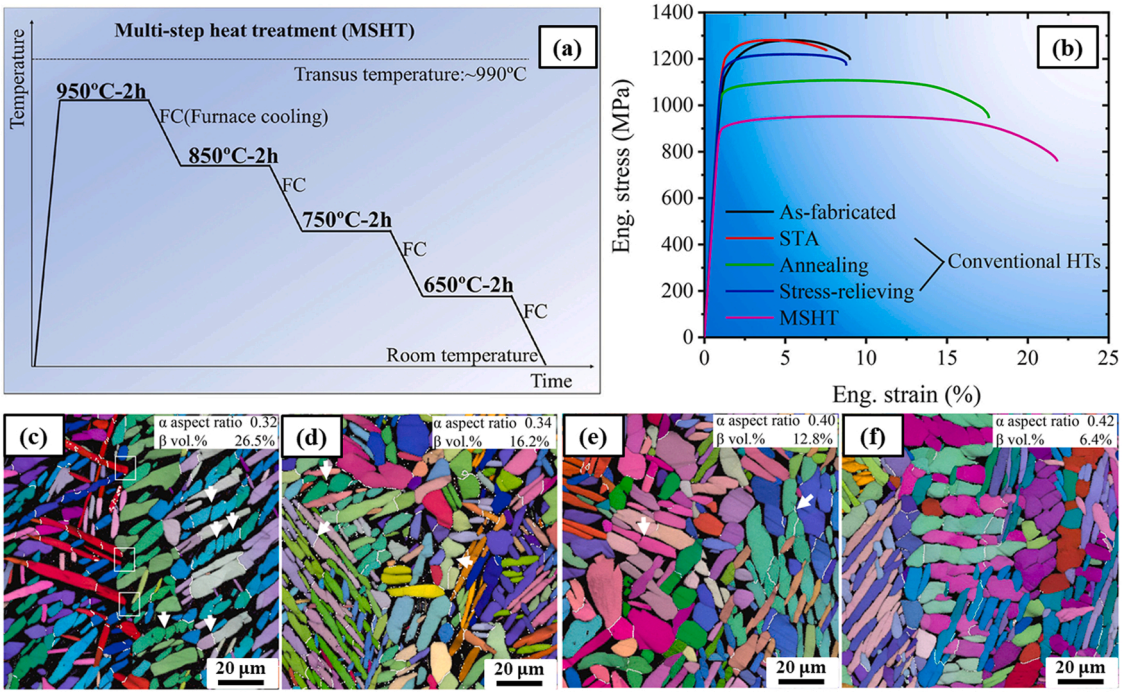

Fig. 4. (a) MSHT cycles of SLM Ti-6Al-4V alloy showing subsequent heat treatments at 950, 850, 750, and 650 °C for 2 h with furnace cooling, (b) tensile properties of MSHTed Ti-6Al-4V compared to other heat treatment processes. Electron backscatter diffraction (EBSD) images of MSHTed Ti-6Al-4V after heat treatment at (c) 950 °C for 2 h and cooled inside the furnace to room temperature, (d) 950 °C for 2 h, cooled to 850 °C, remained at 850 °C for 2 h, and cooled inside the furnace to room temperature, (e) 950 °C for 2 h, cooled to 850 °C, remained at 850 °C for 2 h, cooled to 750 °C, remained at 750 °C for 2 h and cooled inside the furnace to room temperature, (f) 950 °C for 2 h, cooled to 850 °C, remained at 850 °C for 2 h, cooled to 750 °C, remained at 750 °C for 2 h, cooled to 650 °C, remained at 650 °C for 2 h, and cooled inside the furnace to room temperature.
Figure reproduced from [71].

strength-ductility combinations can be achievable by designing the heat treatment.

Sabban et al. [72] developed an innovatively designed globularization heat treatment cycle for SLM Ti-6Al-4V alloy based on a series of heating and cooling cycles between 975 and 875 °C with different heating (1 ℃/min) and cooling (2.5 ℃/min) rates in order to decompose the α′ martensitic phase and attain a bimodal globularized microstructure, as shown in Fig. 5(a,c). Generally, the globularized microstructure in Ti-6Al-4V alloy can be obtained only after plastic deformation. However, the multiple heating/cooling cycles was also able to decompose the α′ martensitic phase into a globular α phase, as shown in Fig. 5(b). This microstructural evolution was attributed to thermal grooving, boundary splitting, as well as oscillating volume fractions of the α and β phases during thermal cycling in synergy with α phase epitaxial growth during the slow cooling rate. This globularization approach enhanced the ductility (18%) while maintaining high ultimate strength (1017 MPa). Fig. 5(d) shows the microstructure of conventional annealed sample which has only a small fraction of globularization at the grain boundary highlighted by the ellipsoid.

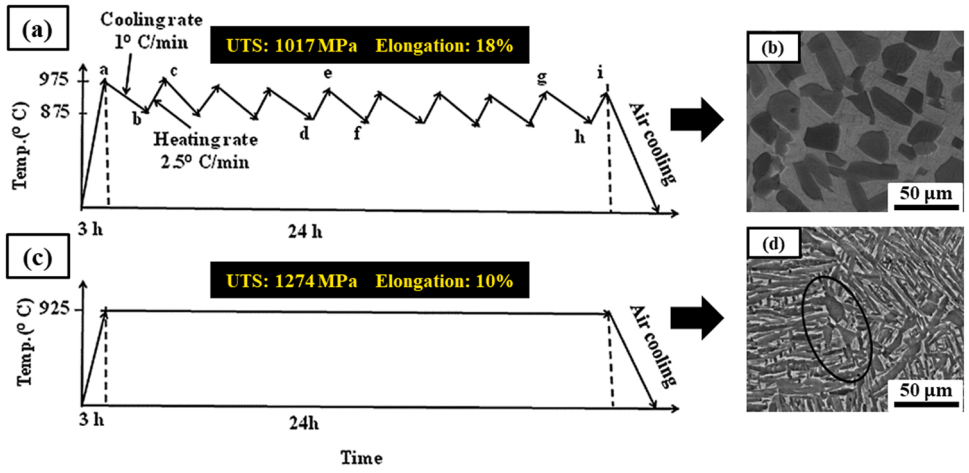

Fig. 5. Innovatively designed globularization (a) heat treatment cycle and, (b) SEM image for SLM Ti-6Al-4 V, (c,d) annealing heat treatment cycle and SEM image for SLM Ti-6Al-4 V. The mechanical properties are inserted in (a) and (c).
Figure reproduced from [72].

Table 2
Mechanical properties of the successful post-fabrication thermomechanical processes on printed Ti-6Al-4V with resultant microstructure.

Manufacturing Method	Thermomechanical Process	Final Microstructure	Mechanical Properties	Ref.
DED	Hot Compression	(α Lath/Platelet) + β	*N.A.	[95]
WAAM	Forging	(Spheroidal α) + β Lamellar (α + β)	MCS: 300 MPa*Strain: 85%	[96]
SLM	Hot Compression	α + β	UTS: 1037 MPa El.: 10.60%	[97]
SLM	Hot Compression	Duplex [α + (α + β)]	MCS: 380 MPa Strain: 90%	[98]
EBM	Hot Compression	α + β	MCS: 28.5 MPa Strain: 75%	[105]
WAAM	Forging	Globularized (α + β)	UTS: 980 MPa El.: 14.5%	[106]
DED	Forging	Globularized (α + β)	MCS: 360 MPa Strain: 90%	[107]
DED	Forging	Globularized (α + β)	UTS: 920 MPa El.: 12%	[108]
WAAM	Single-Step Hot Forging	Lamellar (α + β)	UTS: 1020 MPa El.: 18%	[109]

* N.A.: Not Available, Strain: the amount of strain at failure.

2.2. Post-fabrication thermomechanical processes

In addition to the heat treatment post processes, thermomechanical post processes have gained growing attention in recent years to improve properties of printed parts [86–94]. During the post thermomechanical treatment process, the printed sample is subjected to metal working at high temperatures. Generally, metal working at high temperatures can relieve the residual stresses, eliminate some LOF defects and porosities, and in some cases may also cause recrystallization [95–99]. However, due to the dimensional changes that sometimes occur during thermomechanical methods, achieving a high level of dimensional accuracy in printed specimens is challenging, and hence the parts may require additional post processing procedures such as machining and milling [100–104]. Table 2 summarizes the mechanical properties of some of the post-fabrication thermomechanical processes applied to printed Ti-6Al-4V with their resultant microstructure.

The heat treatment process is able to eliminate the thermal stresses created during AM and decompose the martensite phase (caused by rapid solidification) into α and β phases. However, one of the main challenges in AM methods is the existence of defects such as gas porosity, LOF, and defects in atomized powders that are transferred into the printed part [42,110–114]. Although adjusting the process parameters and finding an optimum parameter range is a possible way to reduce these defects, their complete elimination may not be possible [22,51]. HIP is an efficient method to eliminate these defects by simultaneous application of pressure and temperature [115,116]. As HIP is a thermomechanical process, the recrystallization phenomenon could happen [117–119], which can result in more variety of microstructures and mechanical properties [105,120,121]. Fig. 6(a-f) shows the Ti-6Al-4V microstructures and tensile behaviors made with a conventional manufacturing technique, SLM methods with and without heat treatment and HIP processes [122]. Wrought Ti-6Al-4V has globular α + β microstructure. However, in SLM process, needle-shaped and martensite structures are observed even after heat treatment at 700 ℃. The microstructure is decomposed and partially converted to α and β microstructure by applying a heat treatment at 900 ℃. As indicated by the micrographs in Fig. 6(e), the final microstructure after HIP process is a combination of elongated primary α grains with β phase along grain boundaries. Implementing the HIP process decreased the amount of strength from 1120 to 973 MPa (Fig. 6(f)). However, the amount of elongation is increased to 19%, which can produce high quality samples with properties comparable to conventional wrought Ti-6Al-4V samples.

In Table 3, the mechanical properties and microstructures of HIP Ti-6Al-4V with different AM processes as well as process parameters such as temperature, pressure, duration of the HIP process, and the cooling rate are presented. As clearly shown, by implementing the HIP, the samples exhibited excellent tensile ductility with mostly α + β microstructures, which can produce samples with properties comparable to conventional manufacturing routes (i.e., cast, and wrought Ti-6Al-4V). Besides, experimental findings have shown that applying HIP can improve the fatigue properties of printed Ti-6Al-4V dramatically [40,123–127]. This can be attributed to elimination of the stress concentration locations such as gas porosities and LOFs as well as modification of the microstructure [128,129].

Another post-fabrication thermomechanical process is single-step hot forging which is conducted by Maurya et al.[109] on printed Ti-6Al-4V. They showed that Widmanstätten microstructures in wire arc additive manufacturing (WAAM) process could become α + β and β phase regions after applying a hybrid AM+hot forging process. The macro image and the FEM simulation of the deformed WAAM Ti-6Al-4V at 900 ℃ and strain rate of 0.1 s^{-1} are demonstrated in Fig. 7(a,b), respectively. Their results show that the amount of deformation varies in different regions of the hot deformed Ti-6Al-4V sample making three different deformation zone including plastic deformation zone (PDZ), partial plastic deformation zone (PPDZ), and dead zone (DZ). Fig. 7(A-F) shows the SEM images of microstructure of hot deformed WAAM Ti-6Al-4V specimen from center to the surface as designated in Fig. 7(b). Comparing the microstructures reveals a transition from equiaxed α microstructure for inner regions to lamellar α + β microstructure in outer regions. This indicates that the amount of strain is high in PDZ regions resulting the lamellar α laths transform to equiaxed α phase. Fig. 7(c) demonstrates the tensile properties of as-received, heat treated and hot forged Ti-6Al-4V under different conditions. The results show that by increasing the strain, the amount of elongation decreases. Since strain rate and temperature are considered major parameters in the hot forging process, the authors also studied the effect of strain rates at different temperatures on the microstructure. In Fig. 7(d-i) the inverse pole figure (IPF) with image quality (IQ) maps of the hot deformed WAAM Ti-6Al-4V microstructures at 800 °C, 900 °C and 1000 °C and strain rates of 0.01, 0.1, and 10 s^{-1} are shown. Comparing the microstructures shows that hot forging at 900 °C and strain rate of 1 s^{-1} leads to dynamic recrystallization (DRX). In this condition, almost all the α phases are converted to an equiaxed microstructure. Further increase in temperature (i.e., 1000 °C) beyond the β transus temperature (T_β) results in elongated grain and grain coarsening.

Optimizing process parameters during hot forging can result in mostly equiaxed grains that can exhibit good mechanical properties. However, the components produced with this method will consume more energy which can result in higher production costs. Moreover, due to thermomechanical processes that are applied at high temperatures on parts, maintaining dimensional accuracy is a serious challenge for this approach. Particularly, in this method, hot forging operations are applied only in a single step on the specimens, and the specimen deformation is not uniform in all directions.

2.3. Addition of alloying elements/nucleants

The high cooling rates in AM methods decrease the probability of nucleant formation and equiaxed growth in the melt pool. Therefore, a microstructure with elongated and columnar grains often forms during solidification. Several studies in recent years show that adding specific alloying elements (i.e., La, Cu, Ni, B and Fe) or nanoparticles in very small amounts can play a vital role in creating additional nucleation sites in the melt pool and changing the columnar microstructure to an

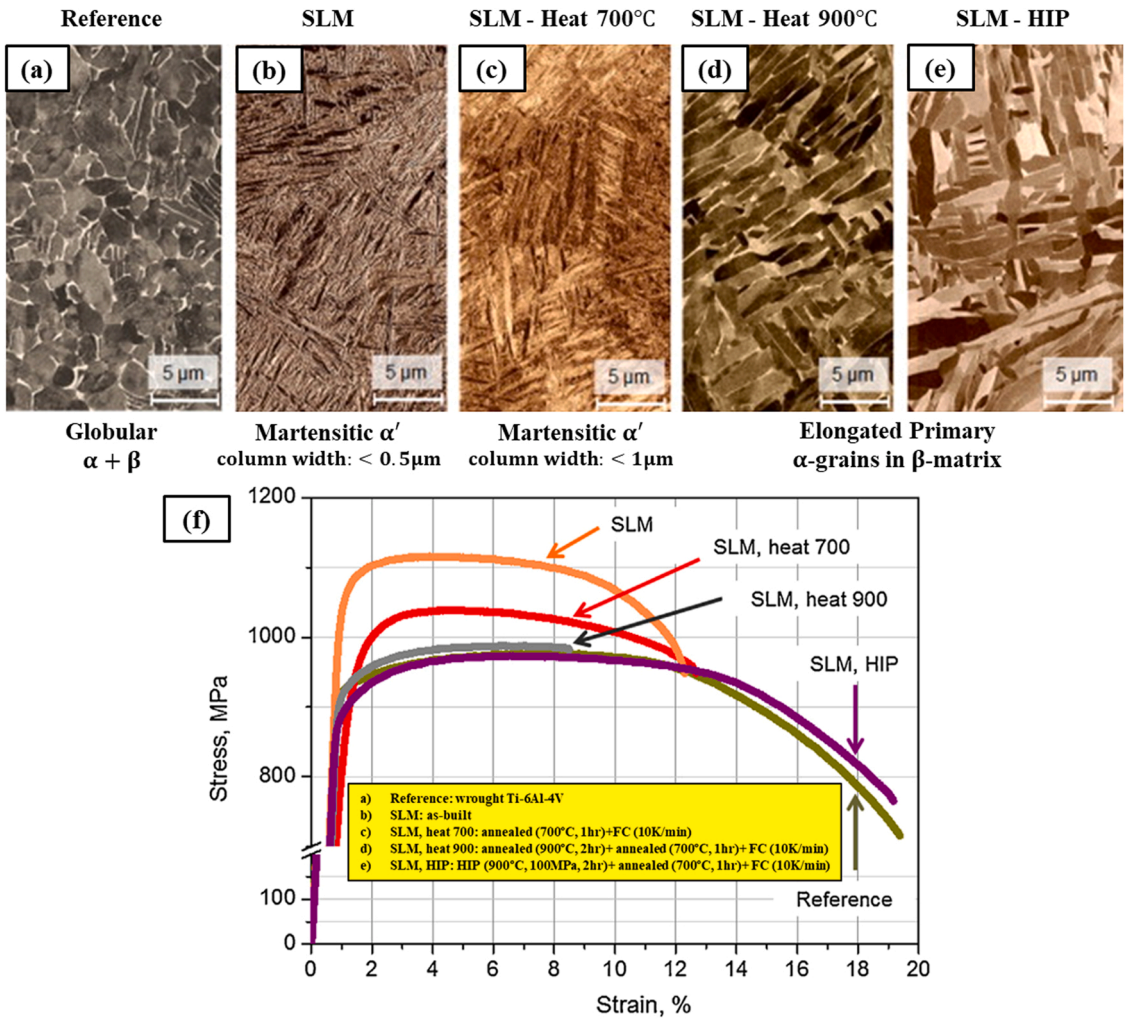

Fig. 6. SEM images of Ti-6Al-4V microstructure with different post processing conditions; (a) wrought Ti-6Al-4V with globular α + β microstructure, (b) SLM with α' martensite (column width: <0.5 μm), (c) SLM and heat treatment at 700 ℃ with α' martensite (column width: <1 μm), (d) SLM and heat treatment at 900 ℃ with elongated primary α grains in β matrix, (e) HIP and heat treatment of SLM parts at 900 ℃ and 700 ℃ respectively with a combination of elongated primary α grains in β matrix and equiaxed grains, and (f) A comparison of stress-strain curves of samples. The inset shows the post processing heat treatment applied to each sample. Figure reproduced from [122].

Table 3
A summary of different HIP schedules applied to printed Ti-6Al-4V to improve mechanical properties.

Manufacturing Method	HIP Temperature	HIP Pressure	HIP Duration	Cooling Rate	Final Microstructure	Mechanical Properties	Ref.
SLM	900 °C	100 MPa	2 h	10 k/min	α + β, α	UTS: 973 MPa El.: 19%	[122]
EBM	920 °C	100 MPa	2 h	–	α + β	UTS: 934 MPa El.: 15.6%	[130]
SLM	930 °C	100 MPa	4 h	10 k/min	α + β	UTS: 938 MPa El.: 14.1%	[131]
EBM	920 °C	120 MPa	2 h	–	α + β, α	UTS: 986 MPa El.: 11.1%	[132]
SLM	920 °C	100 MPa	2 h	0.02 °C/s	α + β	UTS: 1003 MPa El.: 16.1%	[133]
EBM	920 °C	120 MPa	2 h	4 °C/s	α + β	UTS: 1090 MPa El.: 20.1%	[134]
EBM	900 °C	103 MPa	2 h	–	α + β	UTS: 978 MPa El.: 13.5%	[135]

equiaxed one [136–141]. The added alloying element/nucleant can be classified into two general categories: metallic and non-metallic alloying elements/nucleants. The next two sections will review the efforts in this area.

2.3.1. *Metallic alloying elements/nucleants*

Recent studies revealed that the addition of specific metallic elements to the alloy composition during AM process can significantly improve the microstructure and thus the mechanical properties of the alloy. Barriobero-Vila et al. [136] showed that adding small amounts of rare earth metal elements (REE) to Ti can alter the microstructure during SLM. Fig. 8(a) displays part of the Ti-2 wt%La binary phase diagram. Fig. 8(b-g) shows that the addition of La converts the Ti microstructure, which often has needle shape α' martensite structure, into partially equiaxed α grains. Such microstructure transformation is attributed to the $L_1 + \beta \rightarrow La - bcc$ peritectic reaction that occurs during the SLM process [136]. Moreover, comparing the pole figures confirms the reduction of texture in the microstructures after adding La element.

In another study, Zhang et al. [137] investigated the effect of adding Cu, as one of the available and low-cost elements, to pure Ti through direct energy deposited (DED). In addition, this alloy has antibacterial properties due to addition of Cu and making it more attractive for

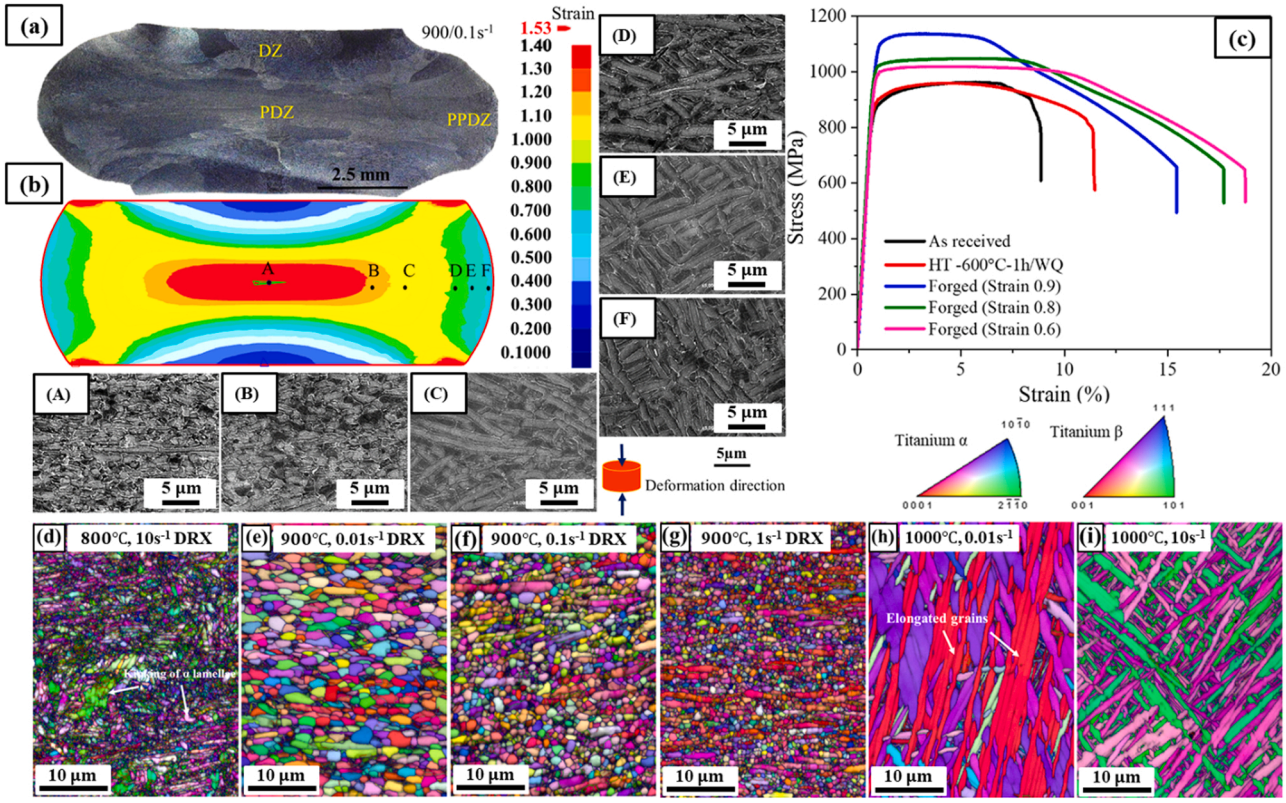

Fig. 7. (a) The macro image, (b) FEM simulated cross-section of the deformed WAAM Ti-6Al-4V at 900 ℃ and strain rate of 0.1 s^{-1} [A-F show the microstructures of specified points from center to surface in (b)], (c) stress-strain curves of as-received, heat treated and hot forged Ti-6Al-4V at different conditions, and the IPF with IQ of the hot deformed WAAM Ti-6Al-4V microstructures at the following temperatures and strain rates: (d) 800 ℃– 10 s^{-1}, (e) 900 ℃– 0.01 s^{-1}, (f) 900 ℃– 0.1 s^{-1}, (g) 900 ℃– 1 s^{-1}, (h) 1000 ℃– 0.01 s^{-1}, (i) 1000 ℃– 10 s^{-1}.
Figure reproduced from [109].

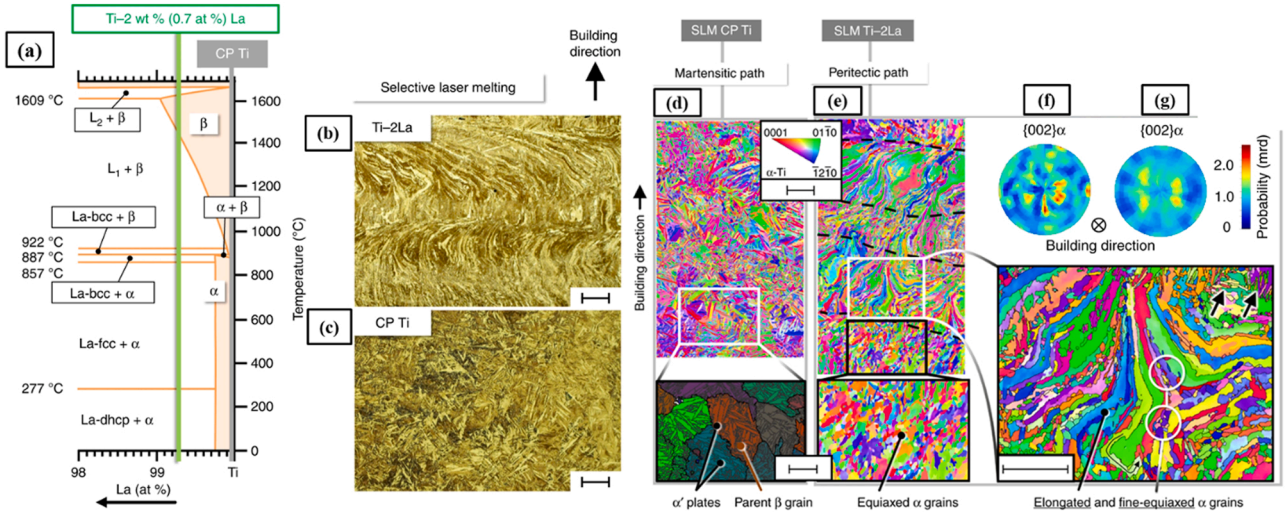

Fig. 8. (a) A part of the binary equilibrium phase diagram of the Ti-La with the specified Ti-2 wt%La composition, (b, c) OM images of the microstructure of SLM Ti-2 wt%La alloy and CP-Ti, respectively. Scale bars in OM images are 100 µm. (d, f) EBSD image and pole figure of SLM CP-Ti to investigate the microstructure of the reference sample, and (e, g) EBSD image and pole figure of the SLM Ti-2 wt%La alloy to investigate the microstructure of the developed alloy. The scale bars in EBSD images and in its magnified regions are 100 µm and 50 µm, respectively.
Figure reproduced from [136].

biomedical applications among different Ti alloys. Fig. 9(a) displays Ti-rich side of the Ti-Cu binary phase diagram. Their results show that by adding 3.5, 6.5, and 8.5 wt% of Cu to Ti, Cu partitioning takes place during the AM process due to a high constitutional supercooling capacity which transforms the columnar microstructure to a more equiaxed microstructure. Fig. 9(b) shows SEM image of the Ti-8.5 wt% Cu with an equiaxed microstructure and ultrafine grains which is a unique microstructure produced for printed Ti alloy. In Fig. 9(c), the grain size is plotted versus the percentage of equiaxed grains for different Ti alloys with different manufacturing routes. As shown,

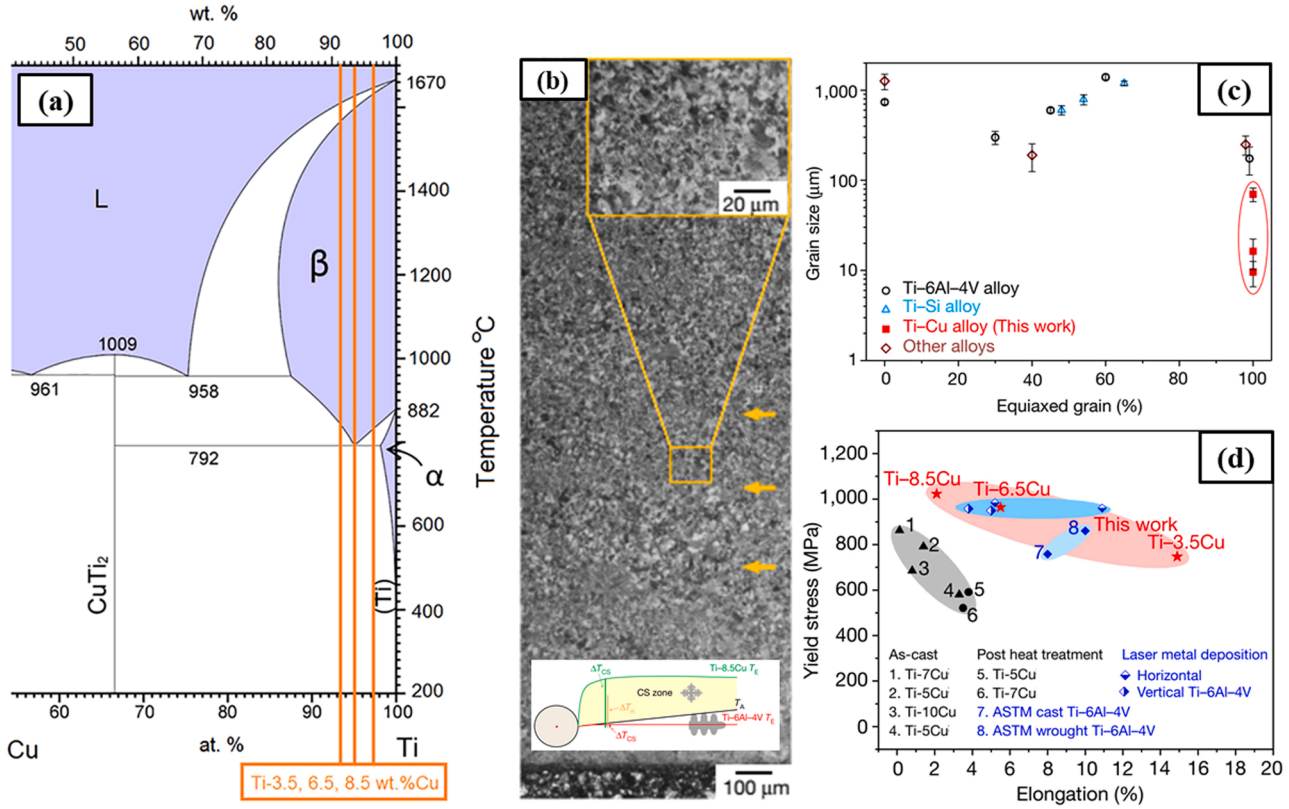

Fig. 9. (a) Ti-rich side of the Ti-Cu binary phase diagram with the specified Ti-3.5, 6.5, 8.5 wt%Cu composition as hypo-eutectoid, eutectoid, and hyper-eutectoid, respectively, (b) OM image of DED Ti-8.5 wt%Cu at low and high magnifications which show uniform and equiaxed grains, (c) grain size diagram versus total percent of equiaxed grains for Ti-3.5, 6.5, 8.5 wt%Cu alloys and other Ti alloys produced by different manufacturing methods, and (d) yield stress diagram versus elongation for DED Ti-3.5, 6.5, 8.5 wt%Cu alloys and other Ti alloys produced by different manufacturing methods.
Figure reproduced from [137].

adding Cu to Ti alloys [137] resulted in a high percentage of equiaxed grains with small grain size, which can lead to a superior strength-ductility synergy as shown in Fig. 9(d).

Recently, Welk et al. [138] studied the effect of different elements on columnar to equiaxed transition (CET) in DED Ti-6Al-4V microstructures. Essentially, by adding these elements, they were trying to increase freezing ranges (ΔT_{fr}) to create significant solutal undercooling during the cooling process. To this end, they first studied the effect of adding various elements on phase diagrams using the Thermo-Calc software. As shown in Fig. 10(a,b), by adding Ni and Fe to Ti-6Al-4V, a significant ΔT_{fr} region is created in the pseudo-binary diagrams. For better comparison of the effect of adding selected elements on the microstructure, Ti samples were produced with and without Ni and Fe addition, and the SEM and EBSD images of microstructures are presented in Fig. 10(c-h). As it is observed, columnar grains and non-equilibrium structures were formed after the DED. However, addition of 3.5% Ni and 6% Fe to the Ti samples, can increase the freezing range and induce a CET during solidification. The results of this study show that the solidification range can be examined in pseudo binary diagrams of Ti alloys utilizing calculation of phase diagrams (CALPHAD) and by choosing the appropriate element, an engineered microstructure can be obtained in the printed Ti. Meanwhile, one of the challenges is that increasing the ΔT_{fr} can cause solidification cracking, so adjusting the amount of the alloying element to reduce the risk of solidification cracking should be taken into consideration.

2.3.2. *Non-metallic alloying elements/nucleants*

The second class of elements added to Ti alloys to alter the microstructure in AM are non-metallic elements/nucleants. To this end, Bermingham et al. [142] investigated the effect of adding Boron (B) to the Ti-6Al-4V alloy during WAAM. Fig. 11(a) and (b) schematically illustrate the solidification diagrams and microstructure patterns for the two Ti-6Al-4V and Ti-6Al-4V-B alloys, respectively. Due to the high reactivity of Ti, B elements react with Ti to form TiB particles. Similarly, Chen et al. [143] reported that by adding the B in WAAM process of Ti-6Al-4V, precipitated TiB particles act as a potent nucleant for the heterogeneous nucleation of the α phase due to the identified specific orientation relationships of $(001)_{TiB}//(0001)_{\alpha}$, $(001)_{TiB}//\{1120\}$ and $(100)_{TiB}//\{1010\}_{\alpha}$ and excellent lattice matches between them. As it is shown in Fig. 11(a) and (b), secondary dendrite arms can form due to the high cooling rate in the AM process. Because of their higher ΔT_{fr}, TiB particles prolong the solidification period, and lateral growth is slowed due to the lateral rejection of boron-rich solute from the base and sides of columnar dendrites. In addition, TiB needle-shaped particles in the molten pool act as nucleation site for the formation of α grains and result in a refined microstructure with respect to pure Ti-6Al-4V. In Fig. 11(c, d), the average width and length size of the α laths for Ti-6Al-4V, Ti-6Al-4V-0.05B, and Ti-6Al-4V-0.13B samples are plotted, respectively. Although the width of the α-laths did not change significantly in the as-deposited condition with the addition of boron, the lath lengths were dramatically reduced by more than four times. This reduction can be attributed to the presence of TiB particles that promoted equiaxed-α formation.

Recent studies investigated the addition of other non-metallic elements/nucleants such as ceramic B_4C and Y_2O_3 into AMed Ti alloys [144,145]. Fereiduni et al. [144] investigated the effect of a trace B_4C addition (0.2 wt%) on the mechanical properties and microstructure of SLM Ti-6Al-4V under as-built and heat-treated conditions. Using B_4C particles during the printing process led to the dissolution of B and the formation of TiB precipitates in Ti-6Al-4V alloy. TiB needles limited the

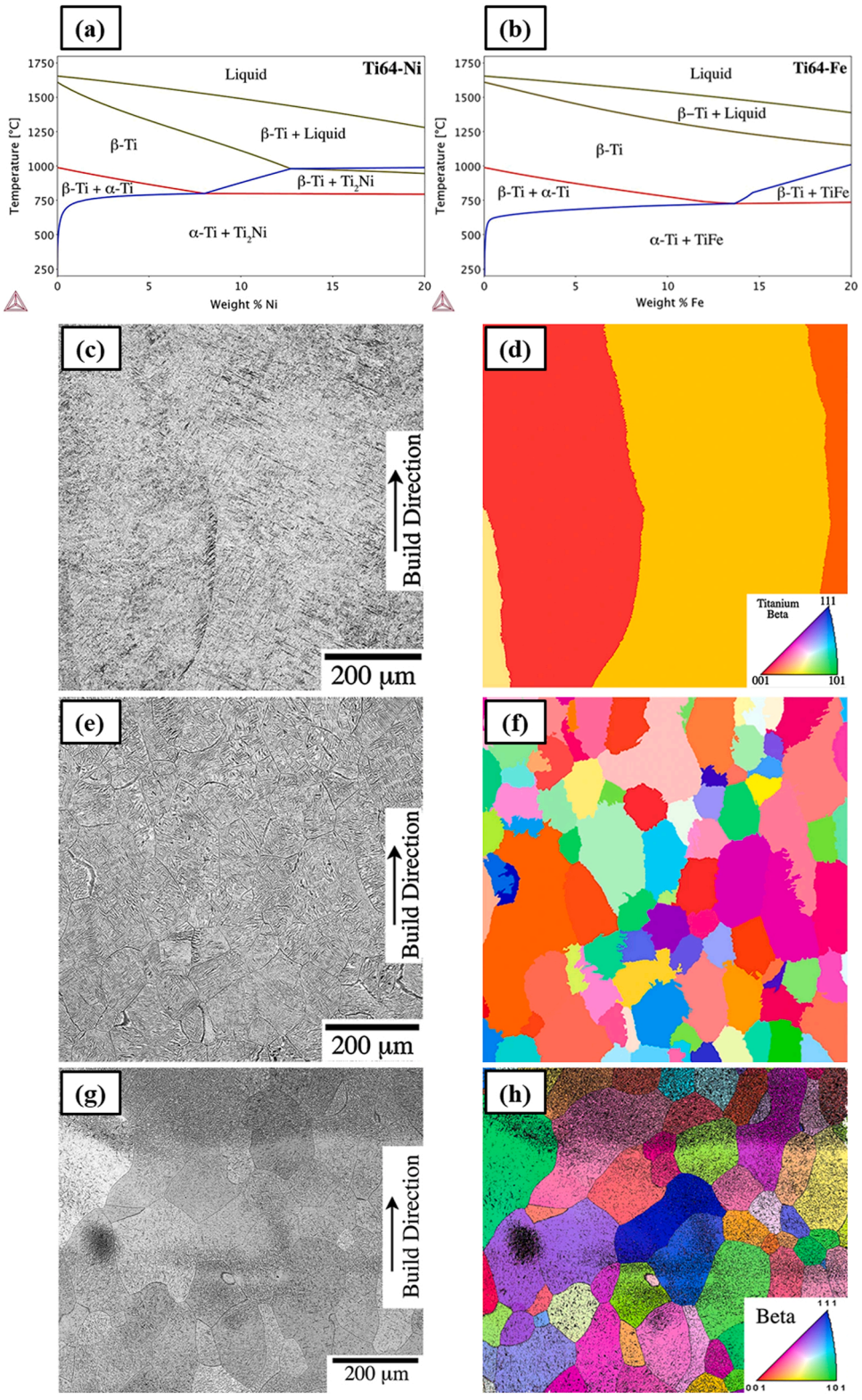

Fig. 10. (a,b). Pseudo-binary phase diagrams using Thermo-Calc software for Ti-6Al-4V alloys with Ni and Fe, (c,d) SEM and EBSD images of the DED Ti-6Al-4V, (e,f) SEM and EBSD images of the DED Ti-6Al-4V microstructure with 3.5% Ni, (g,h) SEM and EBSD images of the DED CP-Ti microstructure with 6% Fe. Figure reproduced from [138].

growth of prior β grains and the nucleation/growth of α phase generated by β→α transformation. Therefore, the presence of TiB leads to a fully isotropic microstructure with a 1400 MPa ultimate tensile strength and a 40% elongation after heat-treatment at 1050 °C without concerns about the deleterious GB-α phase.

Wang et al. [145] studied the precipitation of nano-sized dispersed yttria (Y_2O_3) particles during WAAM of Ti-6Al-4V alloy and analyzed their influence on the shape of the deposited bead, microstructure evolution, and mechanical properties. Fig. 12(a,b) demonstrate the schematic of the microstructural development for WAAM- Ti-6Al-4V

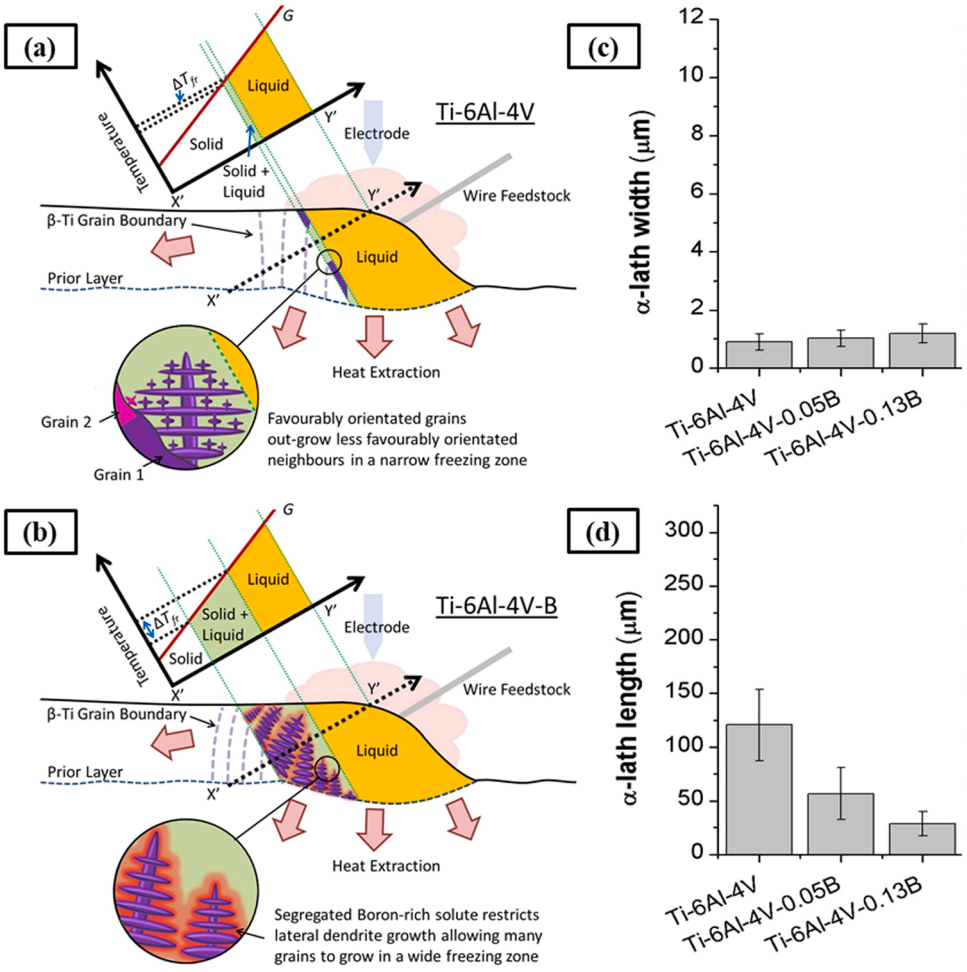

Fig. 11. Schematic of the solidification, grain growth and solid/liquid zones for (a) WAAM Ti-6Al-4 V, and (b) WAAM Ti-6Al-4 V-B alloy. As it can be seen from the two diagrams, the amount of solid/liquid region for the Ti-6Al-4 V-B alloy is larger, which indicates higher ΔT_{fr}. (c) Width and (d) length of the α laths for as-deposited Ti-6Al-4 V, Ti-6Al-4 V-0.05B, and Ti-6Al-4 V-0.13B samples.
Figure reproduced from [142].

without Y_2O_3 addition. As seen, during solidification process, the prior β can grow freely, resulting in larger prior β grains. In addition, because of the wider β grains, the growth of the α phase will be promoted. Fig. 12(c, d) show the bright-field TEM and EBSD images of the deposited Ti-6Al-4V, respectively which confirm the coarse α phase formation. Conversely, the addition of a small quantity of Y_2O_3 (0.22 wt%) to Ti-6Al-4V can modify the microstructure and associated mechanical properties. The Y_2O_3 particles during the solidification process gather at the prior β grain boundaries and can prevent the grain growth. Moreover, narrow β grains can limit the growth of the α phases and the Y_2O_3 particles may additionally serve as nucleation points during solidification. Fig. 12(g,h) show the bright-field TEM and EBSD images of the deposited Ti-6Al-4V with 0.22 wt% Y_2O_3. In WAAM- Ti-6Al-4V/0.22 wt % Y_2O_3 samples, a fine phase was observed, which resulted in grain refinement. Fig. 12(i) illustrates the schematic of the Y_2O_3-restricted grain growth during in-situ thermal cycling during deposition. Typically, the printed layer undergoes multiple temperature cycles throughout the deposition procedure. In situations where the deposited layer encounters temperatures over the β-transus, the primary Y_2O_3 particles impede the movement of grain boundaries. Then, as the printing process continues, the deposited layer experiences temperatures over the recrystallization temperature. In this scenario, the secondary Y_2O_3 particles impede the movement of the α phase migration. Therefore, the resulted microstructure of WAAM- Ti-6Al-4V/0.22 wt% Y_2O_3 will be lamellar α + β. The stress-stain curves of WAAM- Ti-6Al-4V samples without and with Y_2O_3 additions in transverse and longitudinal directions is plotted in Fig. 12(j). Tensile properties of the WAAM-Ti-6Al-4V showed that by increasing the amount of the Y_2O_3 particles from 0.12 wt% to 0.22 wt%, the ultimate tensile strength and elongation of the samples in both of the transverse and longitudinal directions increased. The printed Ti-6Al-4V/0.22% Y_2O_3 sample exhibited the greatest combination of ultimate tensile strength (1180 MPa) and elongation (16%) among the samples.

3. State-of-the-art approaches

The idea of conventional post processing heat treatment methods in AM as a solution to improve the microstructural and mechanical properties is derived from conventional manufacturing routes [29,75,83, 107]. In fact, Ti alloys that are produced by casting or metal working methods are inevitably subjected to post-heat treatment or post-thermomechanical processes to eliminate or minimize α' phase, defects, and porosities in their microstructures. With the increasing trend of using 3D printed parts in different industries, novel techniques are emerging to enhance mechanical properties and tailor microstructure of printed Ti alloys which are discussed below.

3.1. Forced inter-pass cooling

Using reactive atmospheres (i.e., N_2 and CO_2) or N_2 +Ar to change

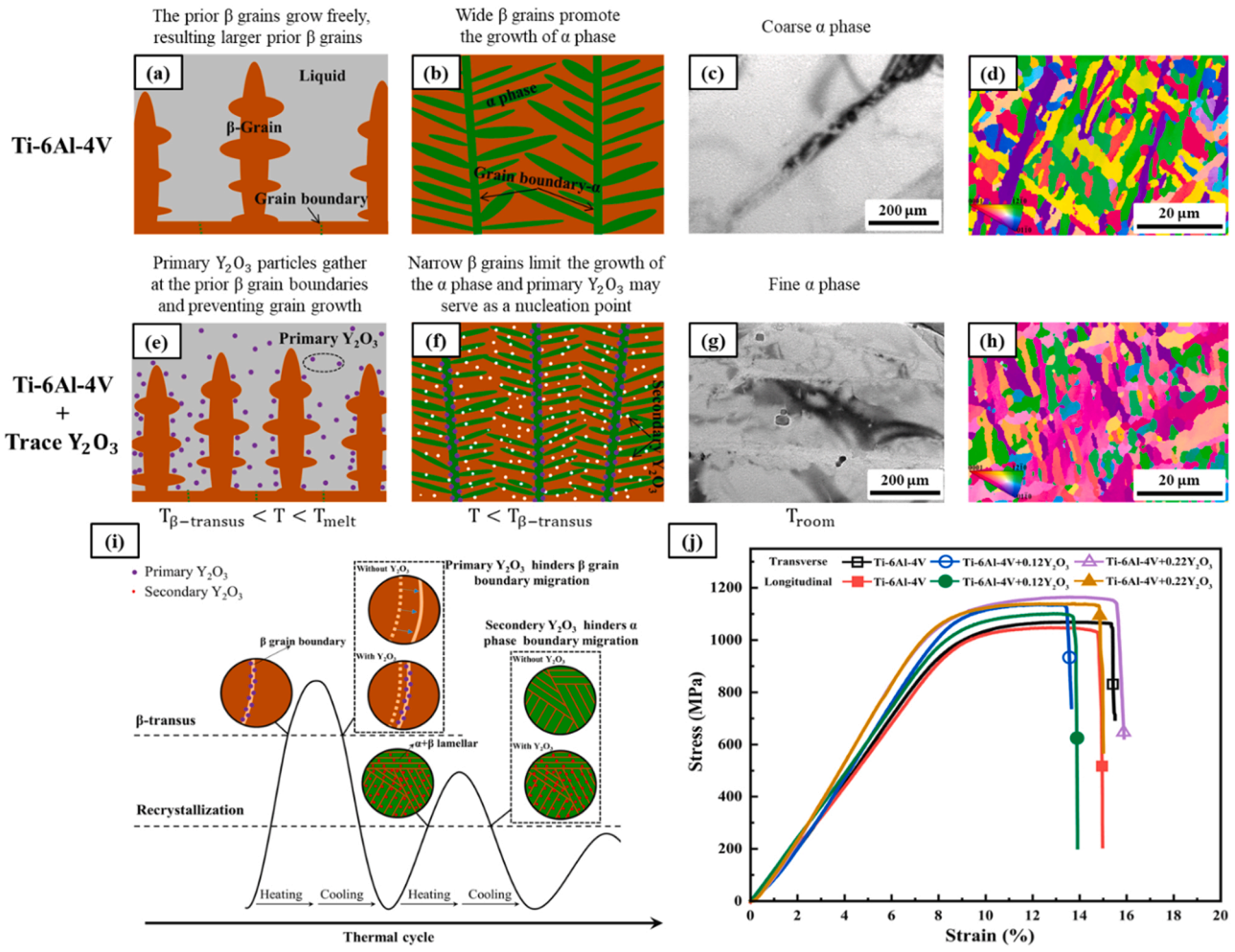

Fig. 12. (a,b). Schematic of the microstructural development for WAAM Ti-6Al-4V without Y_2O_3 addition from high temperature to room temperature, (c) bright-field TEM and (d) EBSD images of the WAAM Ti-6Al-4V without Y_2O_3, (e,f) Schematic of the microstructural development for WAAM Ti-6Al-4V with Y_2O_3 addition from high temperature to room temperature, (g) bright-field TEM and (h) EBSD images of the WAAM Ti-6Al-4V with Y_2O_3, (i) r schematic of Y_2O_3-restricted grain growth during post-deposition thermal cycling, (j) stress-stain curves of WAAM Ti-6Al-4V samples without and with Y_2O_3 additions in transverse and longitudinal directions.
Figure reproduced from [145].

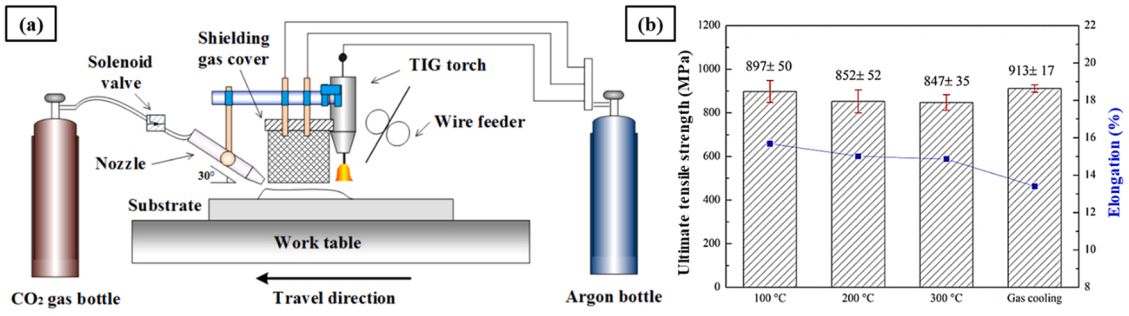

Fig. 13. (a) The schematic of GTAW based WAAM with a commercially available CO_2 cooling spray nozzle, (b) UTS and elongation of GT-WAAM and forced inter-pass CO_2 cooling processes after cooling down to 100 °C, 200 °C, 300 °C and room temperature.
Figure reproduced from [154].

the microstructure during or after depositing a layer has attracted increasing attention in the AM of high-performance Ti-6Al-4V alloy [146–153]. In the forced inter-pass cooling method, the simultaneous combination of an AM process along with the application of CO_2 cooling gas in each layer is proposed by Wu et al.[154]. By implementing this idea, they have tried to decrease the oxidation of layers during the printing process and adjust the inter-pass temperature between each layer to control the microstructure and achieve the desired mechanical properties. Fig. 13(a) depicts the schematic of their setup consisting of gas tungsten arc welding (GTAW) based WAAM combined with a commercially available CO_2 cooling spray nozzle. Considering that the CO_2 gas flow during the GTAW process causes arc disruption, the cooling

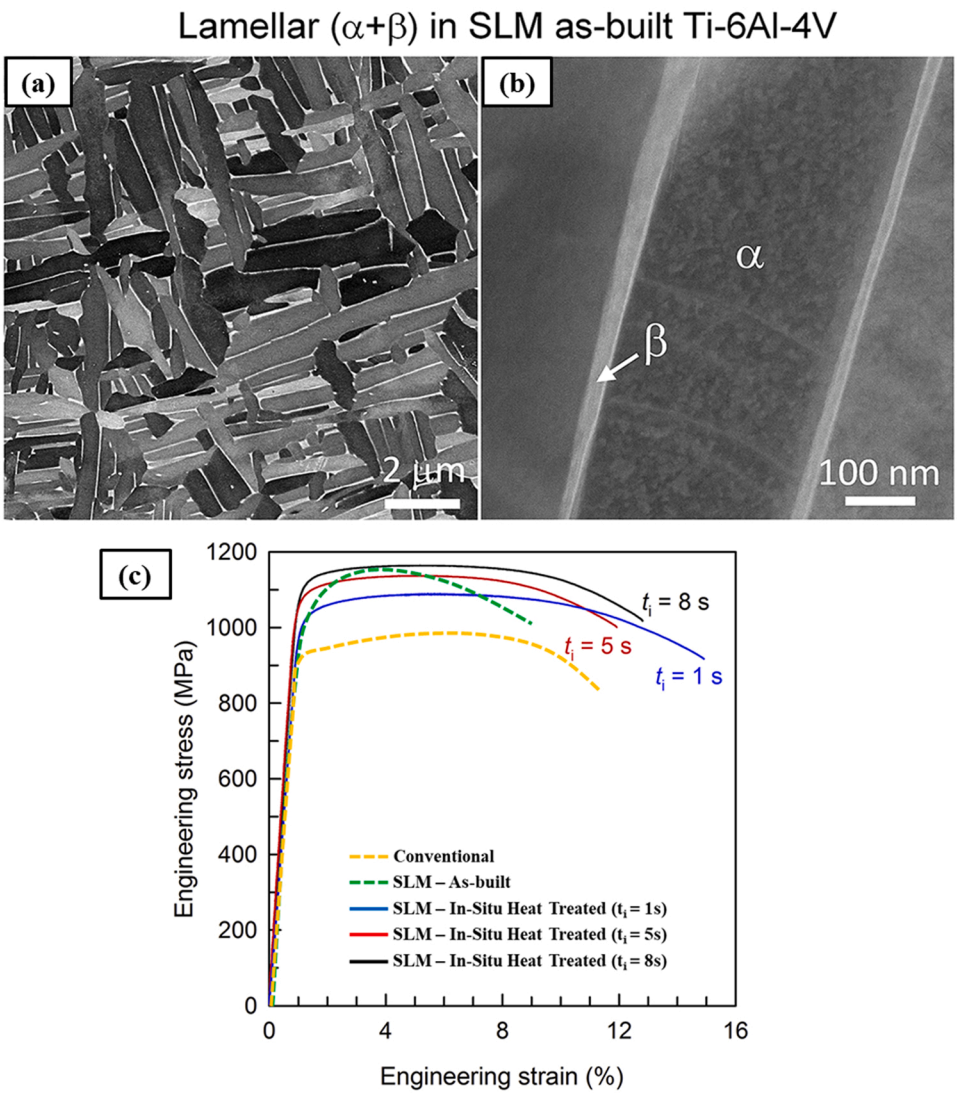

Fig. 14. (a) SEM image of the in-situ heat treated Ti-6Al-4V manufactured by SLM that represents a fully lamellar α +β microstructure, (b) TEM image with higher magnifications to specify the α and β layers. As it can be seen, the darker phase is α and the lighter layer next to it, is the β phase. (c) The stress-strain curve of the in-situ heat treated Ti-6Al-4V sample manufactured by SLM at different inter-layer times of t = 1 s, t = 5 s, and t = 8 s along with conventional mill-annealed and SLM Ti-6Al-4V. Figure reproduced from [156].

process with CO_2 gas is applied after the printing process until the temperature of the deposited layer reaches room temperature. Fig. 13(b) shows the UTS and elongation of the WAAM and forced inter-pass CO_2 cooling processes after cooling down to room temperature, 100 °C, 200 °C, 300 °C with CO_2 gas. Comparing the results show that by decreasing the inter-pass temperature, the UTS increases from 847 MPa to 913 MPa. This is attributed to the refined microstructure of Ti-6Al-4V. By increasing the inter-pass temperature, the elongation slightly decreases potentially due to more oxidation of layers at higher temperatures. Moreover, after forced inter-pass CO_2 cooling to room temperature, the elongation slightly decreased and reached 13.5%, which can be related to the brittle microstructure of α' at higher cooling rates. However, the UTS and elongation of GT-WAAM+ forced inter-pass cooling are still comparable to the conventional manufacturing routes.

3.2. In-situ heat treatment

As previously discussed, in the conventional methods section, regardless of the manufacturing method of Ti alloys, post-heat treatment is still considered as one of the economical and accessible methods to overcome the microstructural challenges in AM [155,156]. One of the capabilities of the AM method (specifically beam-based AM techniques) is use of the deposition beam or an auxiliary beam to reheat the printed layer and conduct an in-situ heat treatment [155,157–159]. More specifically, each powder layer will be melted at a high beam power to create a fully consolidated layer, which will then be promptly reheated by the same or another beam with a low or medium power. In this process one of the crucial factors is the inter-layer time, which is the total heat treatment duration for each layer (t_i). In a recent study, Xu et al. [156] performed in-situ heat treatment with different inter-layer times during SLM of the Ti-6Al-4V alloy. Fig. 14(a,b) show the SEM and TEM images of the lamellar microstructure of α + β in Ti-6Al-4V alloy at high magnification after in-situ heat treatment. These findings show that by implementing in-situ heat treatment, α' martensite could be decomposed into a lamellar α + β microstructure. Fig. 14(c) also shows the engineering strain-stress curve of conventional mill-annealed and SLM Ti-6Al-4V alloys as well as in-situ heat treated samples for 1, 5, and 8 s. In the as-built sample, the high strength and inadequate ductility (total elongation less than 10%) is caused by unfavored α' martensite microstructure. In-situ heat treatment for 1, 5 and 8 s resulted in α + β lamellar structures and the elongation value for each of the three samples was greater than 11% which is the ductility of the conventional Ti alloy. However, by increasing the interlayer time from 1 to 5, then 8 s, the width of the α laths decreased from 0.52 to 0.29, then 0.25 μm. Due to the larger α laths in the in-situ heat treated sample with 1 s interlayer time, the elongation rate increased to its highest level of 12.7 ± 2.1%. Comparing the results reveals that the strength-ductility

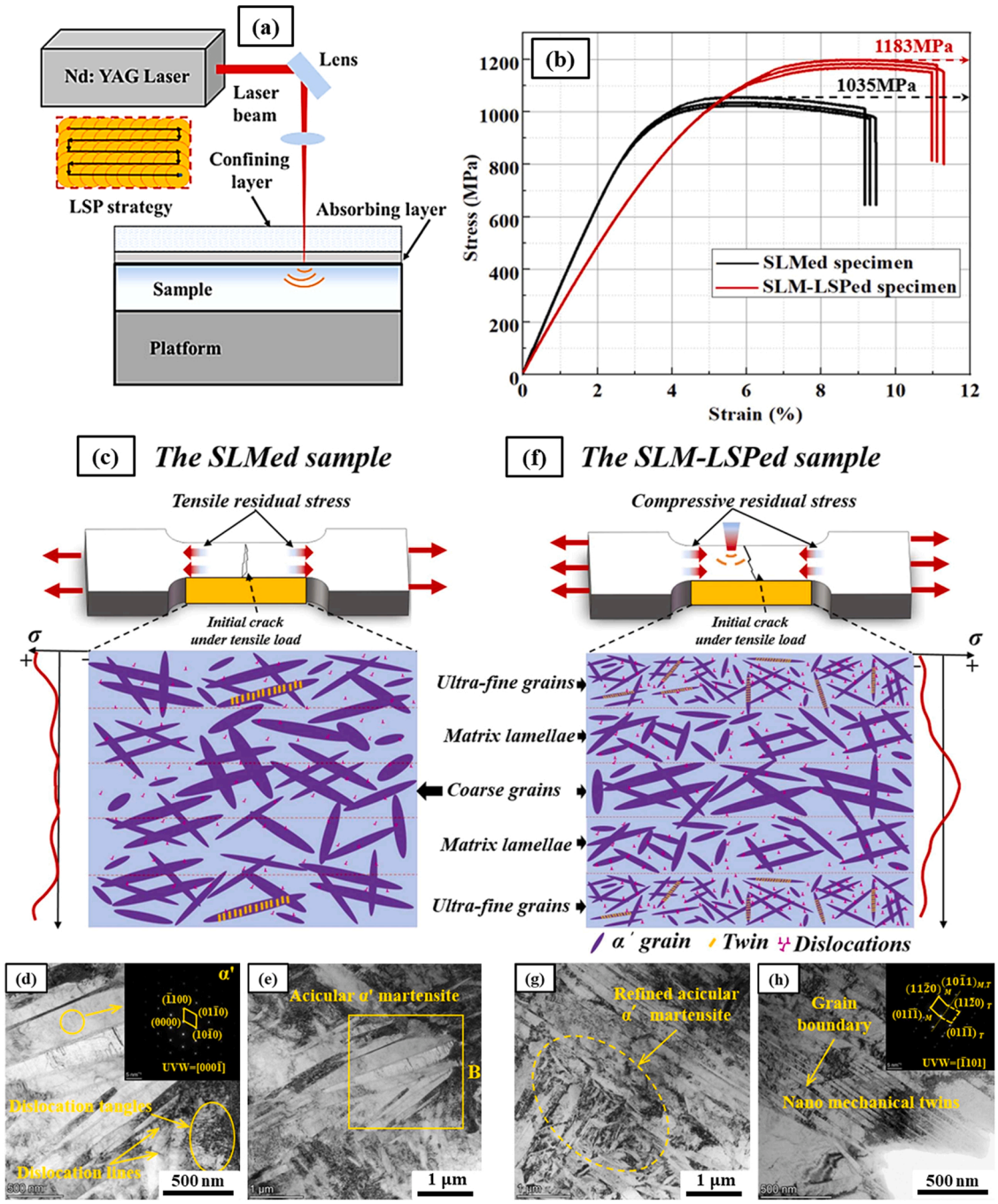

Fig. 15. (a) A schematic of the LSP process to modify the microstructure of the Ti-6Al-4V samples, (b) The stress-strain curves of the SLM and SLM-LSP, and (c-h) the schematic of the SLM and SLM-LSP specimens, respectively to show the mechanism of changing microstructures. These schematics exhibit how the LSP process creates twins and changes the SLM grains to ultra-fine grains. The SEM images at different magnifications show the final microstructures after manufacturing. Figure reproduced from [160].

can be tuned by applying the in-situ heat treatment.

In another recent study, Lu et al. [160] examined the effect of laser shock peening (LSP) on microstructural and mechanical properties. LSP is a surface treatment that induces plastic deformation and compressive residual stress in the material. A schematic of the process is illustrated in Fig. 15(a). In this study, LSP is applied as a post-processing step on SLM printed samples. The results show that by performing the LSP process, the residual tensile stresses, that are often formed after fabrication, are converted into compressive stresses. In addition, as depicted in Fig. 15 (c-h), the LSP process results in a high density of dislocations and a large number of parallel nano mechanical twins in α' microstructure that leads to grain refinement. The results of the tensile test on these samples are plotted in Fig. 15(b). As can be seen, due to the LSP process, the final tensile strength has increased to almost 1200 MPa with the elongation of about 11.5%.

LSP could also be applied during the printing process after single/multiple layer prints. Such approach has been adopted by combining LSP and SLM [161,162]. Applying LSP during SLM process reduced the tensile residual stresses and made a significant improvement in geometrical accuracy of printed parts [163].

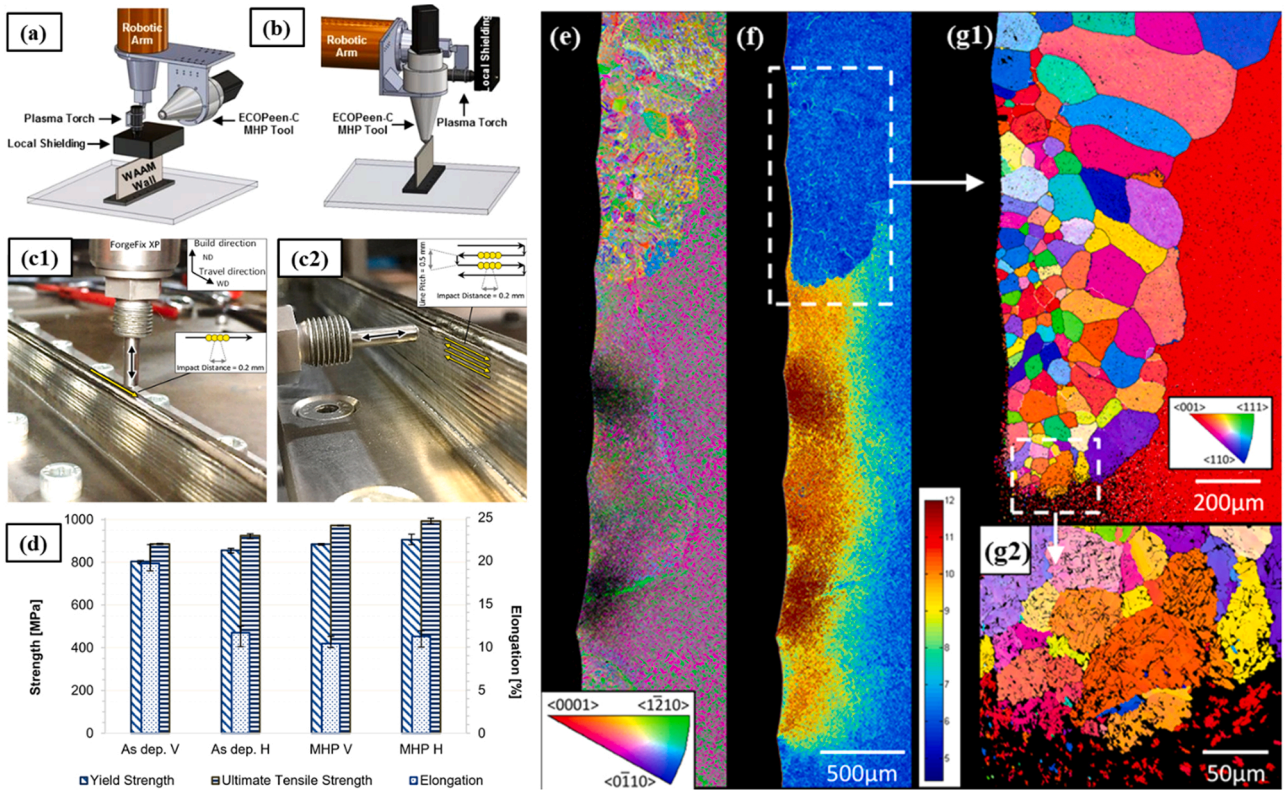

Fig. 16. The Schematic of (a) WAAM, and (b) MHP set-up, MHP tool during [164], (c1) vertical inter-pass peening, and (c2) inter-pass side peening [165], (d) ultimate tensile strength, yield strength, and elongation of as-deposited and MHPed Ti-6Al-4V samples at vertical and horizontal directions [164], (e) EBSD map of the WAAM+MHPed Ti-6Al4 V sample after re-melting its upper left surface, (f) EBSD-local average misorientation (LAM) of the WAAM+MHPed Ti-6Al-4V sample after re-melting the upper left surface, (g1) the reconstructed-β phase of the recrystallized region and (g2) a higher resolution reconstructed-β map of the region highlighted in (g1).
Figures reproduced from [164,165].

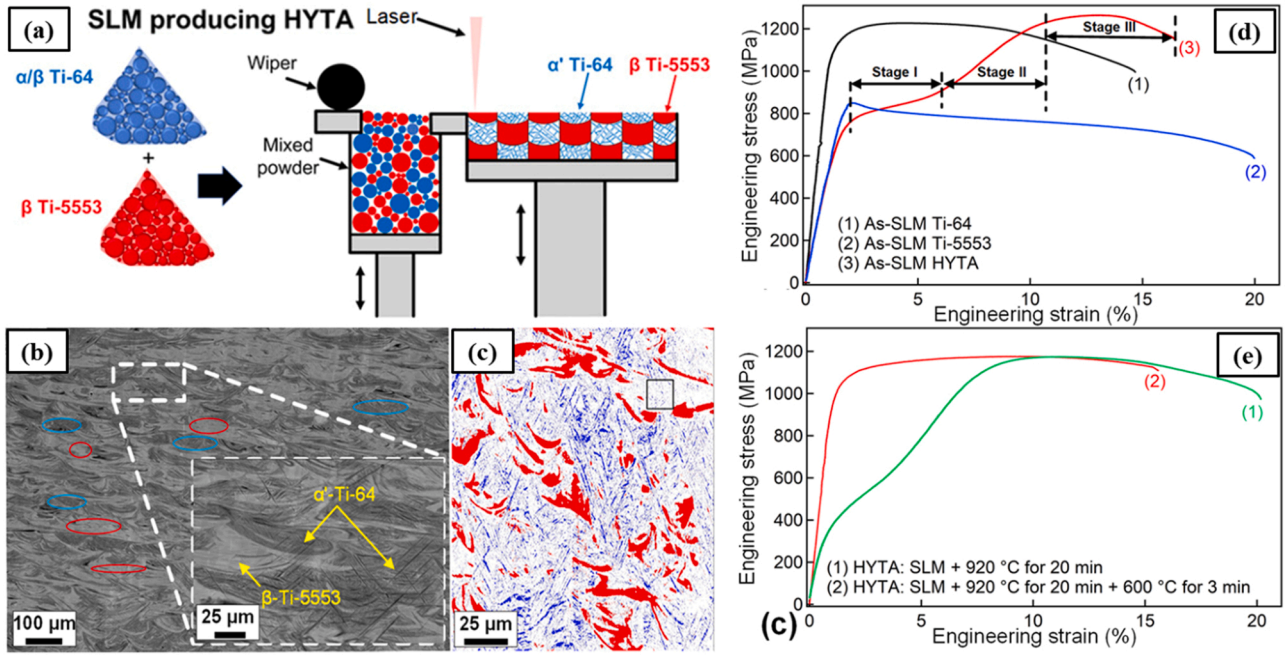

Fig. 17. (a) The schematic of the process of producing Ti samples with a hybridized microstructure indicates how to use two different pre-mixed powders in the SLM process, (b) SEM image of the HYTA sample represent a mixed microstructure of the of α' (marked by blue ellipsoid) and β-Ti5553 (marked by red ellipsoid), (c) EBSD phase-map of Ti5553 (red) and Ti-6Al-4V (blue) showing uniform distribution of these two alloys, (d) strain-stress curve of as-SLM Ti-6Al-4V, Ti5553 as well as resulted HYTA sample after printing, and (e) strain-stress curve for HYTA samples after different heat treatments.
Figure reproduced from [166].

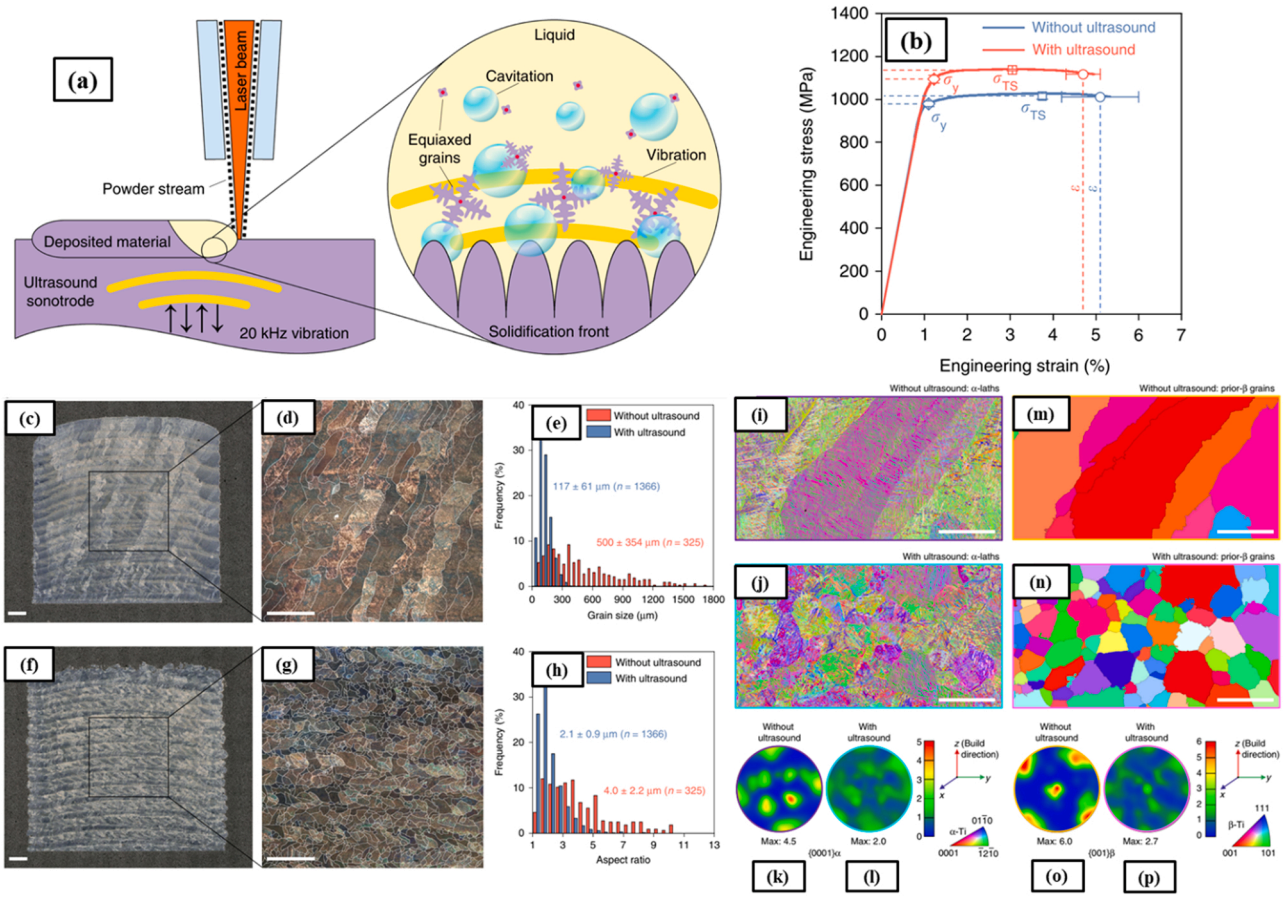

Fig. 18. (a) Schematic of the high-intensity ultrasound process used for DED as well as the effect of high-intensity ultrasound on the nucleation and growth of grains, (b) engineering stress-strain curve of printed Ti-6Al-4V with and without using high-intensity ultrasound process, (c-h) the OM images with different magnifications for printed Ti-6Al-4V samples with and without using high-intensity ultrasound process to show the microstructures along with the prior-β grain size histogram and the prior-β grain aspect ratio for both samples (white scale bars in OM images are 1 mm), and (i-p) the EBSD images and the pole figures of printed Ti-6Al-4V with and without using high-intensity ultrasound process to illustrate the difference in the microstructure of the manufactured samples. Applying high-intensity ultrasound process resulted in a fine and equiaxed microstructure (white scale bars in EBSD images are 250 μm).
Figure reproduced from [167].

3.3. Machine hammer peening

In general, the microstructures of WAAM Ti-6Al-4V samples often have coarse β-grains, which causes strong texture and anisotropy. In recent years, a new technique was introduced by Honnige et al. [164, 165] entitled machine hammer peening (MHP) to overcome the microstructure anisotropy in WAAM. Fig. 16(a,b) show the schematic of WAAM and MHP tool, respectively. Both the WAAM set-up and MHP tool are connected to a robotic arm, which are ready to work with 90-degree rotation after finishing each WAAM or MHP step. Fig. 16(c1,c2) show the MHP tool while applying the vertical inter-pass peening and inter-pass side peening, respectively. The essential parameters for this method are impact distance and line path distances which was chosen as 0.1 mm and 0.5 mm, respectively [165]. The microstructure and mechanical properties of WAAM Ti-6Al-4V samples with and without applying MHP was investigated. The resultant mechanical properties of printed samples in both vertical (V) and horizontal (H) directions are plotted in Fig. 16(d). The results show that in the WAAM Ti-6Al-4V samples, without applying the MHP process, the elongation is anisotropic which can be attributed to columnar prior β-grains formed during the printing process. In contrast, the UTS and yield strength of MHP samples increased to around 1000 and 900 MPa, and the elongation is uniform in both vertical (10.5%) and horizontal (11%) directions and is higher than that of the recommended value of 10% in AMS 4928 standard for wrought samples [164]. They attributed this uniform elongation to grain refinement induced by inter-pass MHP. For microstructural investigations, they printed a wall sample and applied MHP on the left side of the sample. Then, they re-melted the upper left surface of the WAAM+MHP sample with one additional heat source pass. Fig. 16 (e) depict the EBSD map of the WAAM+MHPed Ti-6Al-4V sample after re-melting its upper left surface. Fig. 16(f) demonstrates the EBSD-local average misorientation (LAM) of the same region to show the depth of the deformation induced by MHP. LAM was correlated to local strain values using Finite Element simulation and is what is shown on the scale bar in this map. Fig. 16(g1) and (g2) also show the reconstructed-β phase of the recrystallized region and a higher resolution reconstructed-β map of the region highlighted in (g1), respectively. These characterizations show that after applying re-melting process on the inter-pass side peened regions, refinement of β grain happens in the heavily strained region of the peened layer close to the surface due to recrystallization.

3.4. Hybridizing microstructures

Hybridizing microstructure is another method of manufacturing Ti-6Al-4V samples with tailored microstructure and significant mechanical properties [166]. Fig. 17(a) illustrates a schematic of the hybridizing titanium (HYTA) process. As shown, the α/β Ti-6Al-4V and β Ti-5Al-5V-5Mo-3Cr powders are mixed together and then poured into the powder chamber of the SLM machine. By performing the SLM process, the hybrid microstructure will arise from the initial constituents.

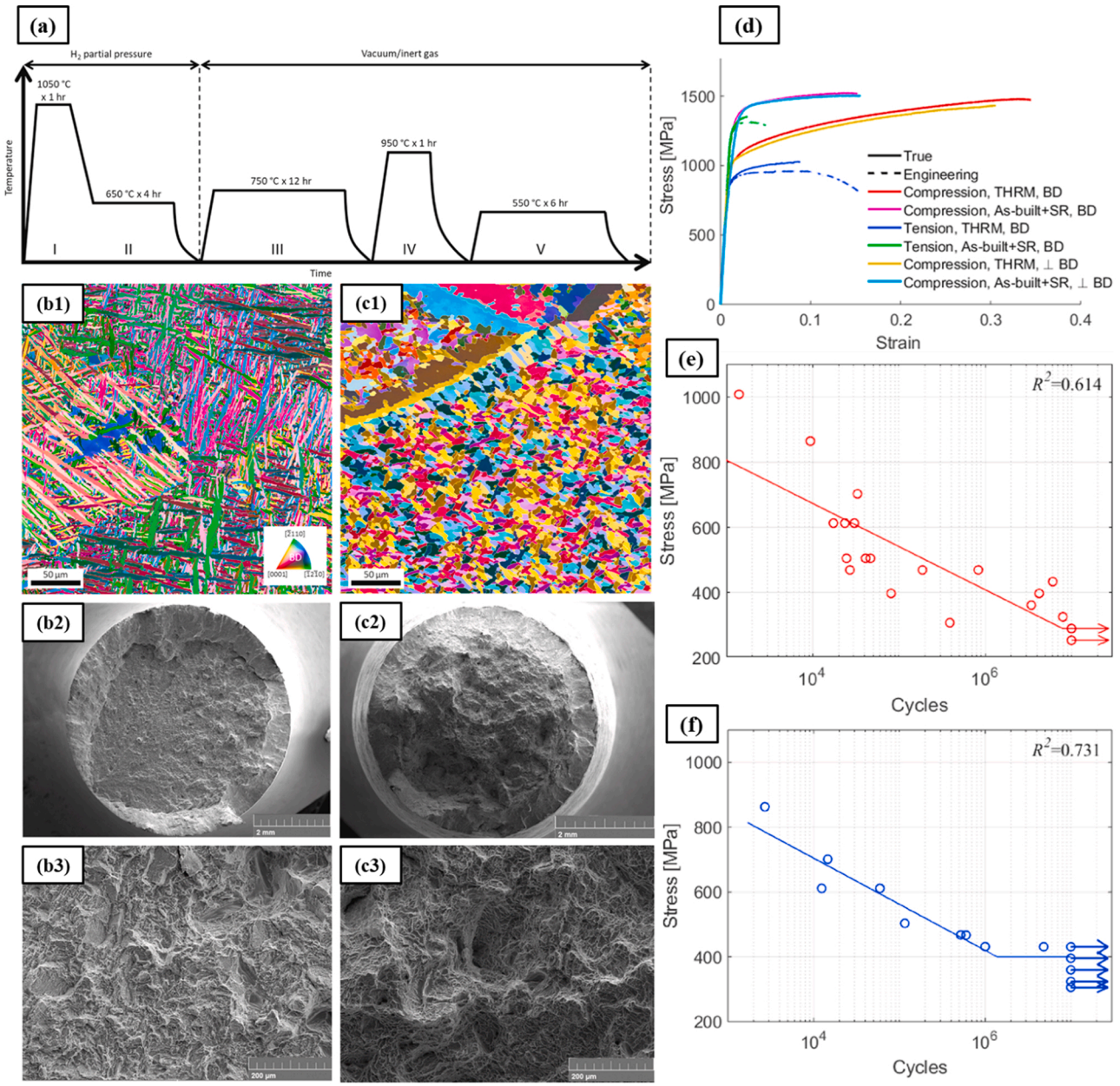

Fig. 19. (a) Temperature versus time diagram showing the THRM and following heat treatment cycle for SLM Ti-6Al-4V, (b1-b3) EBSD and SEM images of as-built Ti-6Al-4V showing the microstructure of the samples as well as the fatigue fracture surface, (c1-c3) EBSD and SEM images of THRMed Ti-6Al-4V showing the microstructure of the samples as well as the fatigue fracture surface, (d) compression and tensile properties of as-built and THRMed Ti-6Al-4V samples at different conditions (BD: built direction and SR: stress relieved), and (e,f) stress versus cycles for fatigue results of as-built and THRMed Ti-6Al-4V samples, respectively. Figure reproduced from [172].

Fig. 17(b) show SEM image of the HYTA sample with a mixed microstructure consisting of the of α' and β-Ti5553 which are marked by blue and red ellipsoids, respectively. EBSD phase-map of Ti5553 (red) and Ti-6Al-4V (blue) after SLM process are also shown in Fig. 17(c) signifying the good mixture of these phases after printing. Fig. 17(d) shows the stress-strain curve of the printed Ti-6Al-4V and Ti5553 alloys as well as HYTA sample after SLM process. Three distinct regions can be observed in the stress-strain curve for HYTA sample which are low work hardening (Stage I), high work hardening (Stage II) and decreasing work hardening followed by necking and fracture (Stage III), respectively. Fig. 17(e) shows that the tensile properties of HYTA samples could be tuned by applying different heat treatments. Heat treatment at 920 °C for 20 min reduced the yield strength, enhanced the work hardening capability, and extended the ductility. However, heat treatment at 920 °C for 20 min followed by subsequent heat treatment at 600 °C for 3 min enhanced the yield strength but eliminated the three stages of deformation.

3.5. *High-intensity ultrasonic vibration*

High-intensity ultrasonic vibration was recently proposed by Todaro et al. [167] to control the microstructure and produce equiaxed grains during DED. A schematic of how the process is performed is provided in Fig. 18(a). By applying high intensity acoustic vibration during the process, the solidified clusters are broken and scattered in the molten pool as nucleants to form equiaxed grains with much smaller sizes. One of the most significant phenomena which occurs during ultrasonic irradiation of liquids is acoustic cavitation. Acoustic cavitation agitates

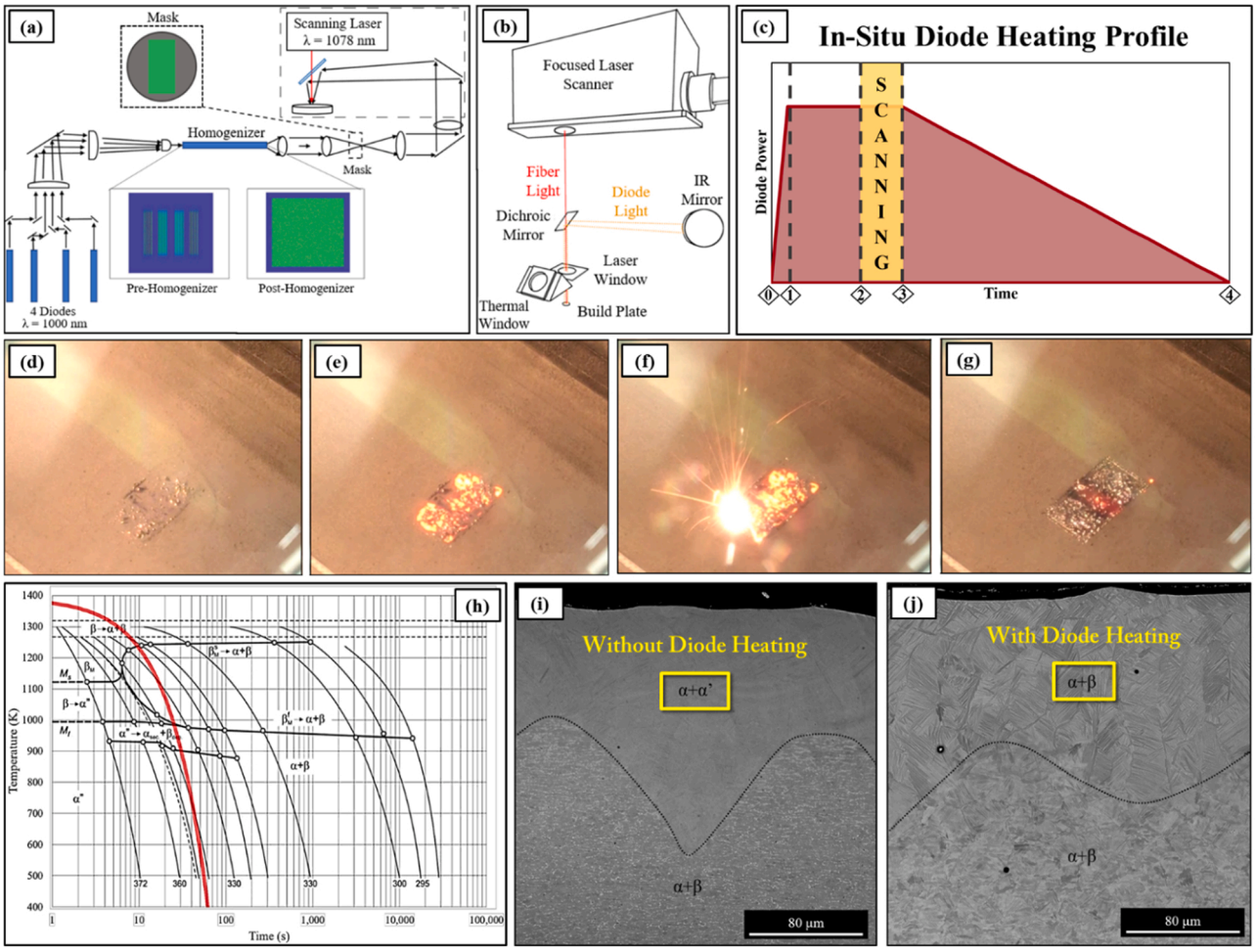

Fig. 20. (a,b) Schematic of developed system with different energy sources in which the first source is nLight scanning fiber laser (1078 nm, 1 kW) and the second one is a set of four Trumpf laser diodes (1000 nm, 1.25 kW each, 5 kW total), (c) in-situ diode heating and scanning profiles for Ti-6Al-4V manufacturing, (d-g) sequence of different steps of applying diode heat and fiber light for pre-heating, printing, and control of cooling rate on each layer, respectively (h) CCT diagram of Ti-6Al-4V alloy associated with cooling curve of SLM Ti-6Al-4V after in-situ diode heating, SEM images of Ti-6Al-4V microstructures (i) without and (j) with in-situ diode heating.
Figure reproduced from [173].

the melt to activate nuclei naturally present in the alloy and has already been implemented in welding [168,169] and traditional casting processes [170,171]. The OM images as well as the measured prior-β grain size and prior-β aspect ratio for Ti-6Al-4V printed samples with and without applying high-intensity acoustic vibration are shown in Fig. 18 (c-h), respectively. Comparing the average prior-β grain size show a considerable reduction from 500 ± 354–117 ± 61 μm after applying the acoustic vibration as shown in Fig. 18(e). Additionally, comparing the prior-β aspect ratio reveal a great reduction from 4.0 ± 2.2–2.1 ± 0.9 as well as shown in Fig. 18 (h). Fig. 18(i,j) and Fig. 18(m,n), respectively demonstrate the EBSD images of α-laths and reconstructed-β phase with and without applying the acoustic vibration. Similarly, a great reduction in the size of prior-β grains and transition from columnar to equiaxed grains can be observed. Moreover, comparing the pole figures in Fig. 18 (k,l) and Fig. 18(o,p) confirms the reduction of texture after employing this approach. The tensile test results in Fig. 18(b) showed that the strength (yield strength, ultimate tensile strength, and fracture strength) has increased without a significant reduction in ductility, which can be attributed to the resultant fine equiaxed microstructure after applying high-intensity acoustic vibration.

3.6. Thermo-hydrogen refinement of microstructure

Thermo-hydrogen refinement of microstructure (THRM) is another idea that has recently been presented to achieve SLM Ti-6Al-4V with engineered microstructure and improved mechanical performance [172]. The main idea of THRM is derived from a powder metallurgy process called hydrogen sintering and phase transformation (HSPT). The HSPT method is a three-step method using dynamically controlled H_2 partial pressures. The first step is β-Ti hydrogen sintering, in which the presence of hydrogen reduces β transus temperature and increases the number of dislocations in Ti-6Al-4V. This step increases the substitutional diffusion of Ti and alloying elements, resulting in high levels of densification (>99%) at moderate temperatures and times. In the second step, hydrogen-enabled phase transformation is used to refine the microstructure, which results in lamellar α colonies and very fine dispersed retained β phase. Finally, the dehydrogenation process under a vacuum or neutral gas environment continues until the amount of remaining hydrogen reaches less than 10 ppm. After doing these steps, samples can be subjected to post-heat treatment cycles to achieve different microstructures such as lamellar, wrought-like globularized, or bi-modal. In Fig. 19(a), a schematic of THRM process in temperature-time diagram shows the sequence of THRM as well as subsequent heat treatment cycles through step I to step V. EBSD images

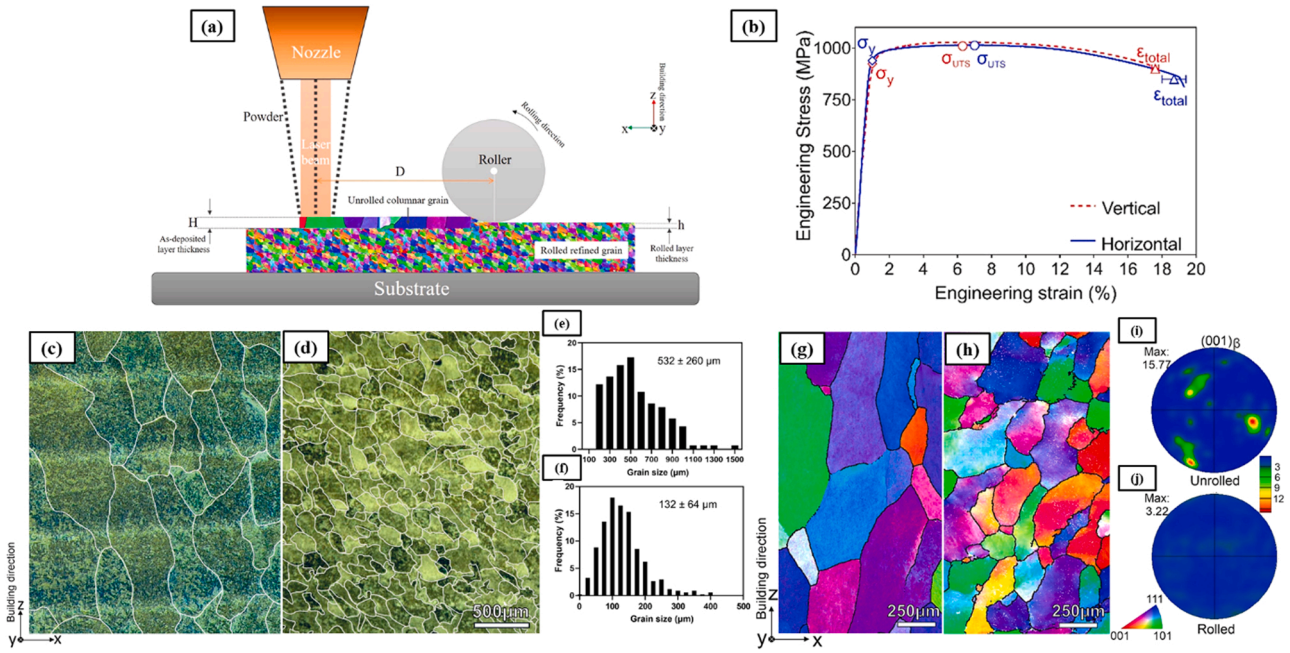

Fig. 21. (a) Schematic of the in-situ rolling process used for DED, (b) engineering stress-strain curve of DED Ti-6Al-4V samples in vertical and horizontal directions, (c-f) the OM images with high magnifications for DED Ti-6Al-4V with and without in-situ rolling process showing changes in the microstructure along with the grain size histogram for both methods, and (g-j) the EBSD images and pole figures of DED Ti-6Al-4V samples with and without in-situ rolling process showing the difference in the microstructure. As it can be seen, applying in-situ rolling process resulted in a fine and equiaxed microstructure.
Figure reproduced from [175].

of microstructure of Ti-6Al-4V with and without THRM process are shown in Fig. 19(b1,c1), respectively. After applying the THRM process, globularized α within prior β are obtained. Fig. 19(d) shows the compression and tensile properties of as-built, stress relieved (SR) and THRMed Ti-6Al-4V samples at different conditions. The samples produced by the THRM technique exhibit a reduction in strength but a considerable amount of elongation. For example, the UTS and elongation of THRMed Ti-6Al-4V samples are 950 MPa and 16%, respectively. They also investigated the fatigue properties of samples as one of the essential properties in engineering applications. Fig. 19(b2-c3) show the fatigue fracture surface of as-built and THRMed Ti-6Al-4V samples at different magnifications. By comparing the fracture surfaces, the THRMed surface shows ductile features, and the fatigue strength of this samples is 400 MPa at 10^7 cycles which is higher than that of as-built Ti-6Al-4V samples with fatigue strength of 285 MPa (Fig. 19(e,f)).

3.7. In-Situ Diode Heating

In-situ diode heating is one of the other state-of-the-art techniques which was recently developed by Smith et. al. [173,174]. In this method, a small-scale custom SLM system was built that uses fiber light for printing and diode light for pre-heating or annealing processes. Fig. 20 (a,b) illustrate a schematic of the developed system where the first energy source is an nLight scanning fiber laser (1078 nm, 1 kW) and second is a set of four Trumpf laser diodes (1000 nm, 1.25 kW each, 5 kW total). As it can be seen from Fig. 20 (c), the diode light provides the energy needeFigd for pre-heating and controlling the cooling rate after the printing process. Then, the fiber light prints the specific areas that should be melted in a layer. The existing setup in this method has the ability to change the order of applying fiber light and diode light; for example, the printing process could be performed with fiber light, and then the annealing process follows with diode light. Fig. 20 (d-g) show the sequence of different steps of applying diode heat and fiber light for pre-heating, printing, and control of cooling rate at each layer, respectively. One of the pivotal factors in the formation of non-equilibrium/metastable phases (i.e., α', α", and ω) and other microstructure defects (i.e., LOF) in the printed samples are the high cooling rates in the AM process. The continuous cooling transformation (CCT) diagram of Ti-6Al-4V alloys is depicted in Fig. 20 (h). The red curve in this diagram is the printed Ti-6Al-4V after applying in-situ diode heating. The cooling rate of this sample reaches approximately to 16 ℃/s, which results in the α + β microstructure. Fig. 20 (i,j) show the resultant Ti-6Al-4V microstructure of printed samples with and without in-situ diode heating, respectively. Results show that using in-situ diode heating process can cause formation of α + β microstructure, which demonstrated the ability of this approach in the production of printed Ti-6Al-4V alloys with tailored microstructure and mechanical properties.

3.8. In-situ rolling

In-situ rolling is one of the techniques which has recently been implemented by Tian et al. [175] to enhance mechanical and microstructural properties of printed alloys. As depicted in Fig. 21(a), in this method, each layer is rolled immediately after the DED method. The distance between the printing beam and the roller (D) as well as the height of the printed layer (H) are of great importance; if these two parameters are not optimized, the microstructure will not transform to the equiaxed grains, and it may damage the layers or may result in defect formations. Fig. 21(b) displays the stress-strain diagram in vertical and horizontal directions for the printed Ti-6Al-4V with in-situ rolling. As it can be seen, the tensile behavior in both directions is almost the same signifying the capability of this approach to reduce anisotropy in printed parts. The achieved UTS and elongation are 1000 MPa and 18%, respectively. Fig. 21(c-j) show the OM, EBSD, and pole figures of the printed Ti-6Al-4V with and without in-situ rolling. Comparing the average prior-β grain size show a considerable reduction from 532 ± 260–132 ± 64 μm after applying the in-situ rolling as shown in Fig. 21 (e,f). Since the printed layer is still at high temperature, the rolling step acts as a thermomechanical process, and, as a result, recrystallization phenomenon induces equiaxed grains. Moreover, comparing the pole figures confirms the reduction of texture after employing the in-situ

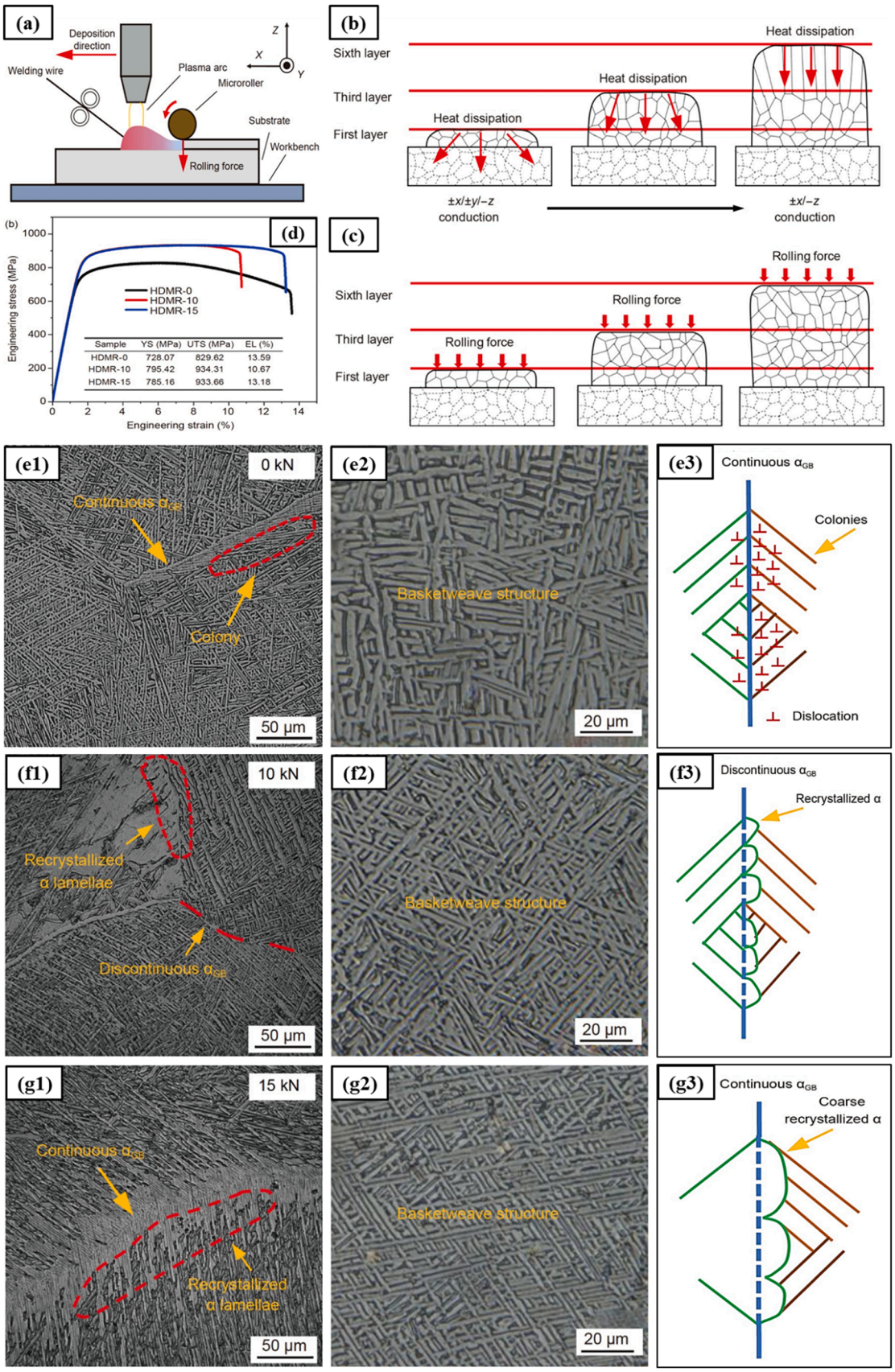

Fig. 22. (a) Schematic of the hybrid plasma-arc deposition and microrolling process, (b) formation of grains in microstructure of WAAM Ti-6Al-4V, (c) formation of grains in microstructure of WAAM Ti-6Al-4V after applying the microrolling process, (d) engineering stress-strain curves of WAAM Ti-6Al-4V after microrolling at different rolling loads, (e1-g2) SEM images of the microstructure of WAAM Ti-6Al-4V after Microrolling at different rolling loads in different magnification, and (e3-

g3) schematic illustrations of changes around α_{GB} after microrolling at different rolling loads.
Figure reproduced from [176].

rolling process.

In-situ rolling has been applied to other AM techniques such as WAAM [176–184]. One of the most recent studies in this field was conducted by Cheng et al. [176]. Fig. 22(a) shows a schematic of hybrid plasma-arc deposition and microrolling method. As can be seen from Fig. 22(b,c), after applying the microrolling process on each layer, the applied force by the roller causes hot deformation, which results in equiaxed grains in the microstructure that are completely different from the columnar grains caused by directional heat dissipation in conventionally printed samples. One of the parameters that is essential in this process is the force (F) applied by the roller. In this research, the effect of different applied forces (i.e., 0, 10, 15 kN) by roller on the microstructure and mechanical behavior of WAAM samples were examined. Fig. 22 (d) shows that by applying the roller force of 15 kN, maximum UTS and elongation can be obtained which are 934 MPa and 13.2%, respectively. The microstructure of samples with different applied rolling loads is shown in Fig. 22(e1-g2) which demonstrates a basketweave of α and β. However, comparing the microstructure in Fig. 22(e1-g1) shows differences in α grain boundaries (α_{GB}); by increasing the applied force, the α_{GB} grain boundaries changed from continuous to discontinuous and the colonies of piled-up dislocations at α_{GB} grain boundaries converted to recrystallized α and coarse recrystallized α as shown schematically in Fig. 22(e3-g3).

3.9. Additive friction stir deposition of recycled metal

Additive friction stir deposition (AFSD) is one of the most recent AM methods [185,186]. In this technique, unlike many AM methods, there are no melting and solidification processes, and therefore it is considered as a non-beam-based metal AM process [187–191]. In fact, the main idea of this AM method originated from friction stir welding (FSW) and friction stir processing (FSP) [192–194]. In the FSW or FSP, the work piece is often placed on the table and fixed by the clamps. A rotating tool typically made of tungsten carbide or steel is connected to the CNC or milling machine, which can move in a transverse direction with respect to the workpiece while rotating around its axis [195–197]. This rotating tool is inserted into the workpiece and due to severe plastic deformation, causes grain refinement in the workpiece [198,199]. The AFSD and FSW/FSP processes have similar concepts, but in AFSD process the rotating tool is made of the material to be deposited on to the substrate or previous layer. In this method, the friction force and severe plastic deformation leads to the material flow, and the final piece is produced by repeating this process layer by layer. The filler material or raw material plays a crucial role in FSWD. One of the ideas that has recently been used in developing this method is the use of metal chips as raw material [200] as shown schematically in Fig. 23(a). As it can be seen in Fig. 23(b,c), a defect-free Ti-6Al-4V sample is produced by the AFSD technique. SEM, EBSD, and pole figures of cross section of AFSDed Ti-6Al-4V samples are demonstrated in Fig. 23(e1-g3). The microstructure of samples shows gradual prior β grain refinement by moving to the bottom of the AFSD Ti-6Al-4V samples. The main grain refinement mechanism in this method is DRX, often dominant phenomenon of grain refinement in severe plastic deformation processes like FSP. The fine grains at the bottom of the sample can be attributed to a) the higher cooling rates at lower part of the samples; In other words, by depositing the new layers in the AFSD process, the temperature of the AFSD can increase due to the friction and severe plastic deformation which reduces the cooling rate and b) higher accumulative plastic strain at bottom layers. Fig. 23(d) shows the stress-strain curve of the AFSD Ti-6Al-4V samples in different sections of the build. The results show that by moving along the build direction, the tensile strength decreased while the elongation increased, which is consistent with the microstructural changes.

3.10. Deliberately introducing LOF defects to drive recrystallization during subsequent HIP

Due to the wide range of machine parameters, design parameters and raw materials in 3D printing methods, there is often the possibility of defect formation such as LOF in the printed parts [201–203]. So far, in almost all manufacturing processes, the LOF has been supposed as a defect, and efforts have been made to prevent the formation of these defects as much as possible by optimizing manufacturing parameters [204–208]. However, in the most recent study, Bustillos et al. [209] exploited LOF defects to obtain SLM Ti-6Al-4V alloy with superior strength-ductility synergy while applying subsequent HIP. Fig. 24(a) illustrates the laser power and scanning speed parameter ranges along with the OM images of samples showing the possibility of LOF defect formation during SLM. As demonstrated, decreasing the laser power and increasing its speed (which essentially corresponds to lower energy density) results in higher density of LOF, and decreasing the laser speed and increasing its power (essentially corresponds to higher energy density), results in keyhole defect. The process parameters and the distribution of LOF in the selected sample for LOF-HIP post processing is shown in Fig. 24(a) with a red box. Moreover, the green box in this figure refers to optimum power and scanning speed to get a fully dense (FD) specimen. Fig. 24(b,c) show the tensile behavior of the LOF-HIP and FD-HIP samples and the comparison with the results available in the open literature. As can be seen, the idea adopted in this research has resulted in a combination of excellent tensile strength and elongation, which matches or exceeds the results obtained from conventional manufacturing methods. The improvement in properties is associated with formation of duplex microstructure. Fig. 24(d-j) illustrate the mechanism for achieving duplex microstructure, along with OM images of the final microstructure for the fully dense (FD) samples, FD with subsequent sub-transus (HIP 1) and super-transus (HIP 2) at 900 and 1000 °C, as well as the LOF with subsequent sub-transus (HIP 1) and super-transus (HIP 2) at 900 and 1000 °C, respectively. They showed during HIP, LOF defects play the main role in creating duplex microstructure based on two phenomena: 1. reduction of high energy surfaces will result in the release of excess free energy lowering the energy barrier for heterogenous nucleation of stress-free α grains and 2. local dislocation-driven recrystallization resulting from the closure of LOF defects. The resultant duplex microstructure results in mechanical properties that surpasses the properties of wrought, cast, solution treated and aged Ti-6Al-4V samples and unveils the capability of this approach in AM Ti alloys for engineering applications.

As it is shown, defects are not necessarily harmful, and they can be exploited for a variety of purposes. To this end, Moridi et al. [210] intentionally introduced pores during printing of Ti-6Al-4V to make porous structures for biomedical applications. Such porous structures can be designed to reduce the elastic modulus of the implant to reduce stress shielding effect while providing space for bone ingrowth. They used a solid-state AM process called cold spray [211] to overcome the challenges associated with the high temperature processing of metals. Their findings show that by implementing the supersonic particle deposition in cold spray process and controlling the processing parameters to be just blow the typical window of deposition, mechanically robust and porous Ti-6Al-4V prints with apparent modulus of 51.7 ± 3.2 GPa, apparent compressive yield strength of 535 ± 35 MPa and porosity of 30 ± 2% can be obtained.

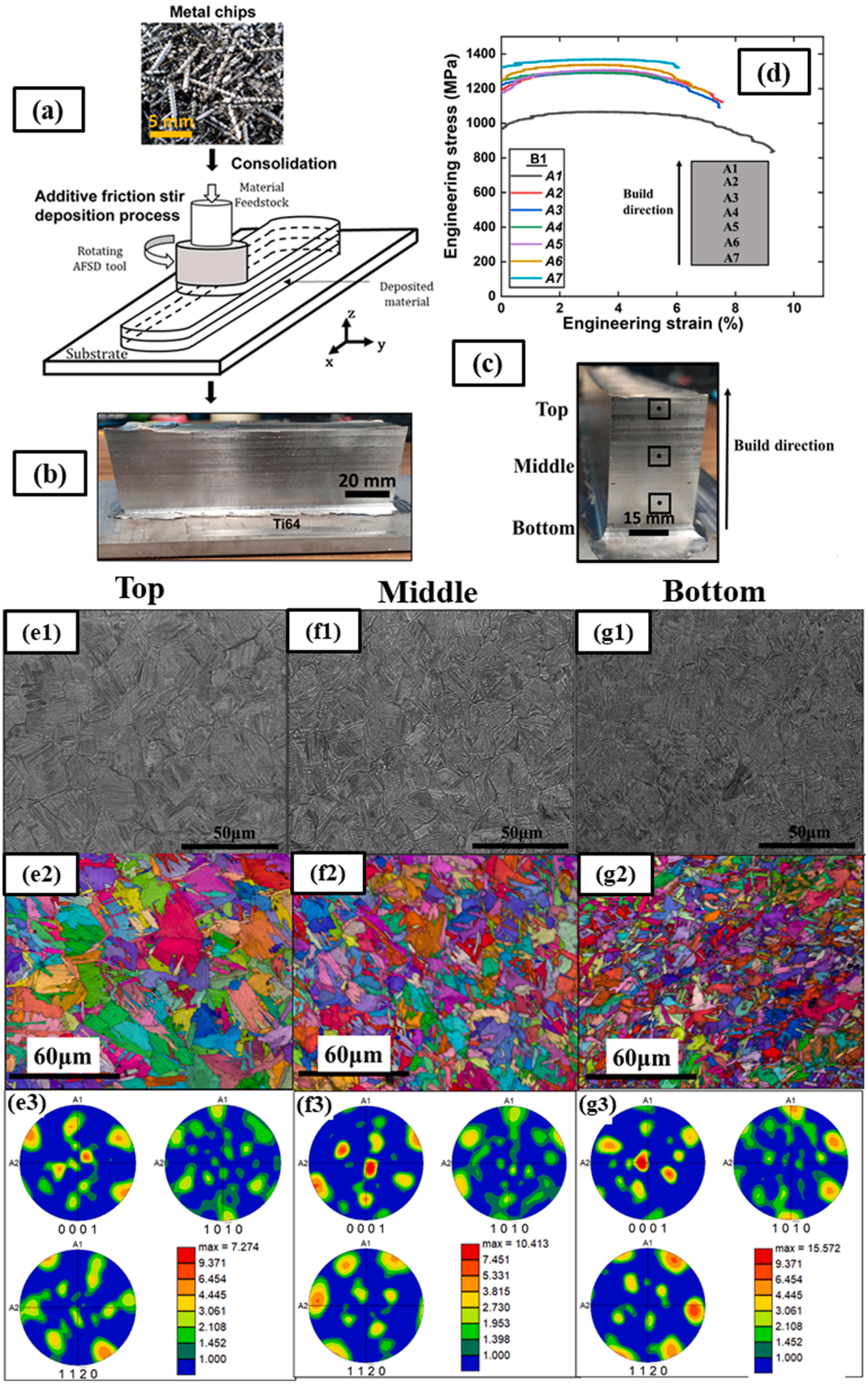

Fig. 23. (a) Schematic of the AFSD process with metal chips as raw material, (b) defect-free AFSD Ti-6Al-4V samples along the longitudinal direction, (c) cross section of the AFSD Ti-6Al-4V samples with specified areas in top, middle, and bottom of the samples for microstructural analysis, (d) mechanical properties of the AFSD Ti-6Al-4V samples in different sections of the build (from bottom to top), (e1-g1) SEM, and (e2-g3) EBSD images as well as pole figures of AFSD Ti-6Al-4V

samples in build direction (from top to bottom) showing fine and equiaxed prior β grains with fine α/β laths in it.
Figure reproduced from [200].

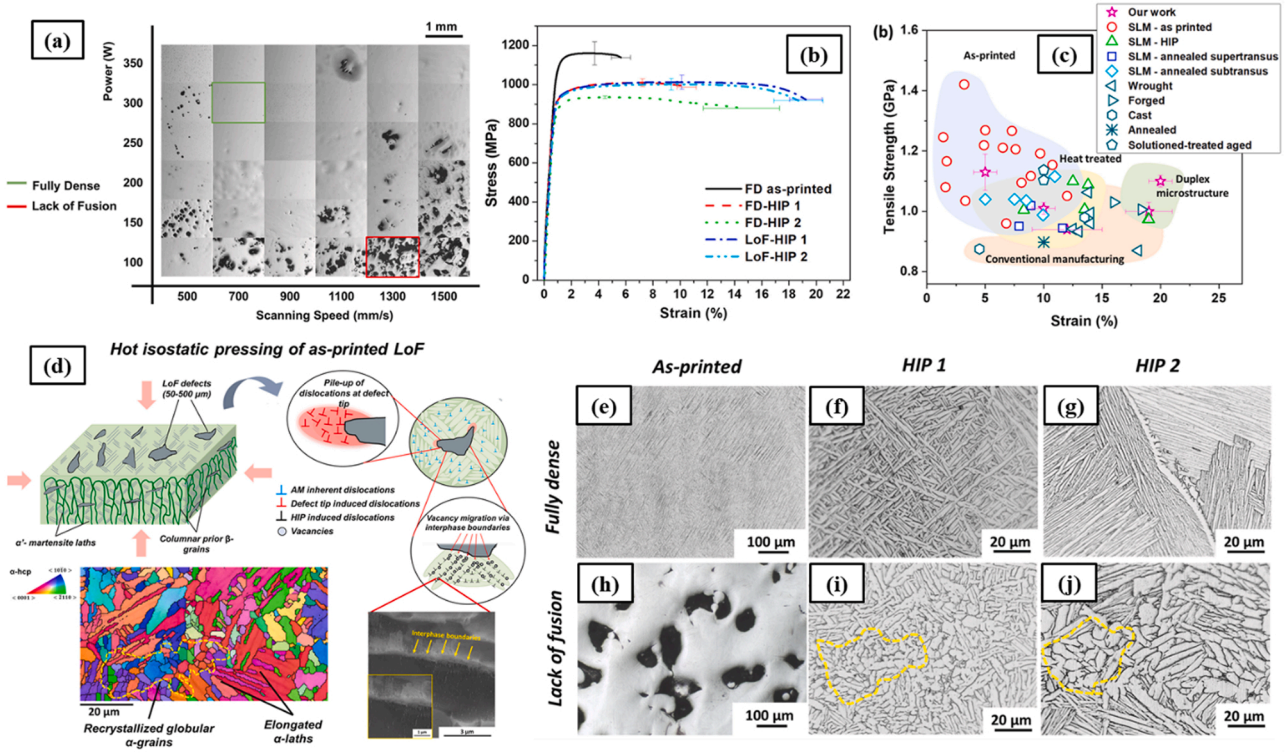

Fig. 24. (a) Processing map for SLM Ti-6Al-4V alloy for different values for laser power and scanning speed, (b) the stress-strain curves for FD sample, HIP 1, and super-transus HIP 2 at 900 and 1000 °C, respectively, as well as the LOF with subsequent sub-transus HIP 1, and super-transus HIP 2 at 900 and 1000 °C, respectively, (c) comparison of tensile strength and strain in the Ashby plot format with wrought, forged, cast, annealed, and other available literature on printing Ti-6Al-4V alloy, (d) a schematic representation for mechanism of microstructural changes during the HIP process of LOF samples, (e-j) OM images of the aforementioned samples showing lamellar microstructure for as-printed and FD-HIP samples and duplex microstructure for LOF with subsequent HIP processing.
Figure reproduced from [209].

3.11. Alternating current assisted wire arc additive manufacturing

Using an alternating current (AC) during WAAM has been proposed by Huang et al. to modify the microstructure of printed Ti-6Al-4V [212]. They altered the columnar microstructure of WAAM- Ti-6Al-4V through modifying the flow behavior of the molten pool during solidification by generating a magnetic field. Fig. 25(a,b) illustrates the experimental set up for WAAM process, the AC current added on the filling wire, and the schematic of the liquid phase flow during AC-assisted WAAM. As shown in Fig. 25(b), when alternating current was applied, a coupling AC arc is developed, which resulted in periodic magnetic arc oscillations of the Tungsten Inert Gas (TIG) arc. The periodic oscillation of the TIG arc subsequently affected the heat distribution, pressure, and molten flow, resulting in several forces in the molten pool, including buoyancy effects owing to temperature differences, surface tension owing to temperature differences (Marangoni effect), and shear forces due to the flow of the arc plasma. In addition, the insertion of alternating current produces an alternating magnetic field in the molten pool which has a substantial effect on solidification. In fact, magnetic fields may significantly lower crystallization temperature. The schematics of the grain growth of WAAM- Ti-6Al-4V with and without the application of AC are represented in Fig. 25(c). The magnetic field led to grain refinement as a consequence of an increase in grain nucleation caused by vigorous stirring in the molten pool. Changing the value of AC and its effect on resulted microstructure and tensile properties were investigated. Fig. 25 (d) shows that the highest AC value of 30 A resulted in the greatest elongation of 10.22%, with a strength of 650.2 MPa. This was attributed to the efficiency of the applied AC at higher levels (30 A), to effectively change the microstructure of the deposited layers from basketweave microstructure to refined equiaxed grains as shown in EBSD maps presented in Fig. 25(e-h).

3.12. Alloy design by surface engineered feedstocks

Zhang et al. [213] have recently introduced a surface engineering strategy to modify the feedstock for SLM. In contrast to other studies, which has mostly focused on grain refinement (via alloy design) and/or defect prevention (through processing optimization), their study reveals that tackling phase heterogeneity is crucial for achieving spatially uniform microstructure and mechanical properties. Fig. 26(a-c) illustrate the feedstock preparation procedure for Ti-6Al-4V, CP-Ti, and Fe_2O_3 using the surface engineering methodology. In this approach, a layer-by-layer assembly method is employed to generate doped titanium feedstock with Fe_2O_3. Their design concept is inspired by decreasing the V content with a low tracer diffusivity in Ti-6Al-4V through introducing a much stronger partitioning element, such as Fe, Ni, or Co, the diffusivities of which are almost two orders of magnitude higher than V. It is then reasonable to expect that significant elemental partitioning can occur during the cooling process, resulting in the in-situ formation of the desired lamellar (α + β) microstructures instead of α′ martensite, which is produced by diffusionless transformation. By using Fe_2O_3, Fe with a greater diffusivity was substituted by V with a lower diffusivity, and the O induced the solid solution strengthening. Fig. 26(d) shows a schematic of the SLM process along with accumulation of thermal cycles in each

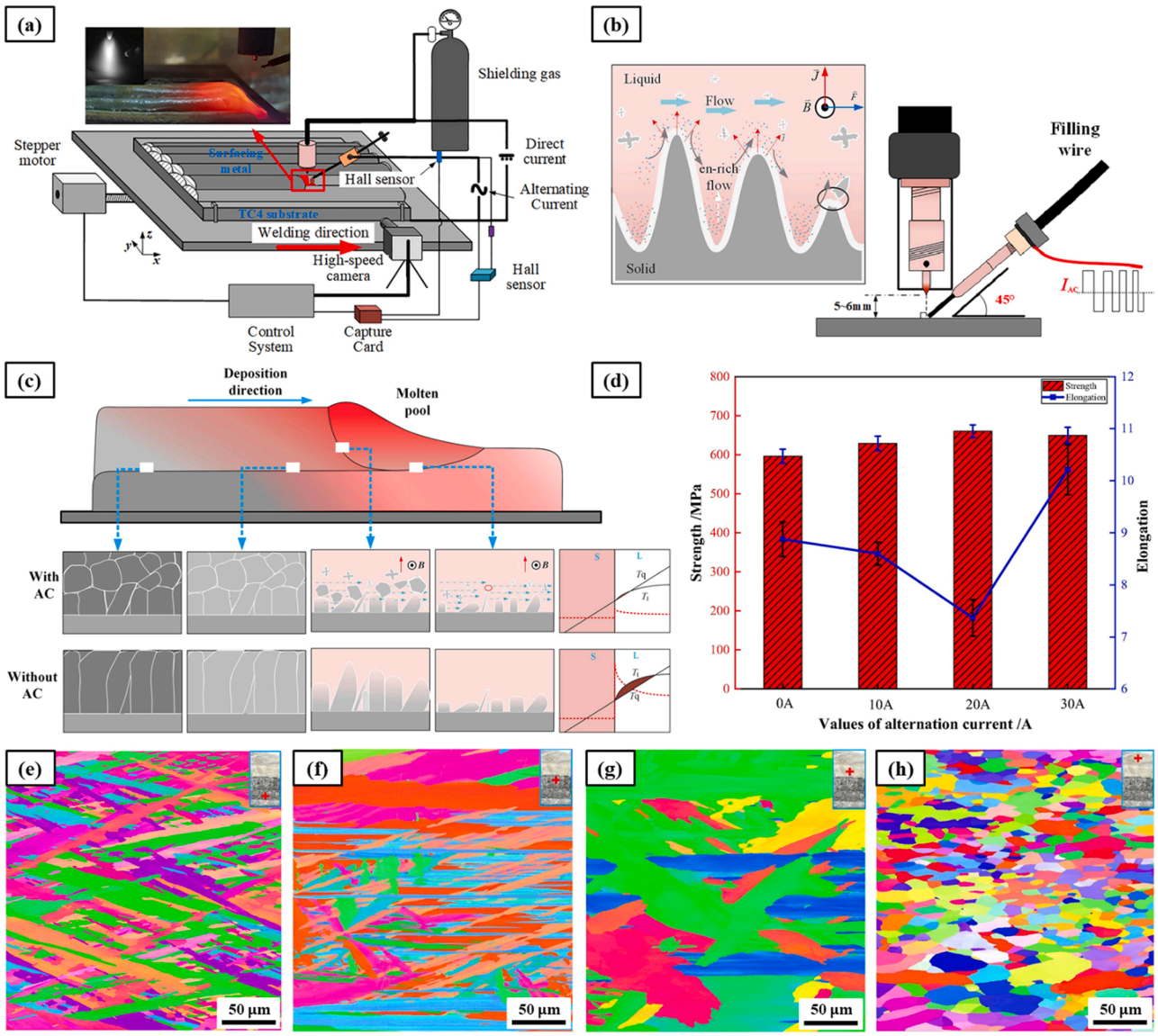

Fig. 25. (a) Experimental set up for alternating current assisted WAAM Ti-6Al-4V process, (b) the AC current added on filling wire and the schematic of the liquid phase flow during AC-assisted WAAM, (c) The schematics of the grain growth of WAAMed Ti-6Al-4V with and without the application of AC, (d) tensile properties of the WAAMed Ti-6Al-4V with different values of the AC, (e-f) EBSD images of the WAAMed Ti-6Al-4V at different AC values of 0 A, 10 A, 20 A, 30 A, respectively. Figure reproduced from [212].

layer. Fig. 26(e1-e3) depict the SEM images of the microstructure of the SLM Ti-6Al-4V samples at different build heights. As shown, the top layer (region A) consists of primarily α' martensitic phase, which is a result of the rapid cooling rate during the SLM process. In the layer corresponding to region B, some of the α' martensitic phase transforms to α and β lamellar structures due to repeated heat cycles as subsequent layers are being printed. Due to the thermal cycles induced by the continuation of the printing process, the microstructure of region C is completely altered to lamellar α + β. Fig. 26(e4) represents the stress-strain curves of horizontal and vertical SLM Ti-6Al-4V samples. As can be observed in Fig. 26(e1-e3), due to the non-uniformity of the microstructure in different regions of the printed samples, the mechanical properties of the printed sample will be anisotropic and different in different directions. Fig. 26(f1-f3) shows the SEM images of the microstructure of the SLM 25Ti-0.25 O alloy, which consists of 25 wt % CP-Ti and 0.25 wt% Fe_2O_3 additions (henceforth referred to as 25Ti 0.25 O, and other newly produced alloys are designated in the same way). Comparing the microstructures of 25Ti-0.25 O and SLM Ti-6Al-4V samples reveals lamellar α + β features in each of the A, B, and C regions. This homogeneity in the microstructure demonstrates the great independence of the designed alloy from the temperature cycles generated during the printing process. Fig. 26(f4) also exhibits the horizontal and vertical stress-strain curves of SLM 25Ti-0.25 O samples. The stress-strain curves of this sample reveal that the tensile behavior of 25Ti-0.25 O is isotropic, with a significant amount of elongation in the range of 16–18.2% and an ultimate tensile strength of around 1170–1200 MPa. The authors also investigated addition of various amounts of CP-Ti and Fe_2O_3 and its impact on mechanical performance. Their results showed that by increasing the value of CP-Ti to the 25, 50, and 75 wt%, the ultimate tensile strength decreases from around 1230–900 MPa and the elongation increases from around 15–28%. In addition, similar to 25Ti− 0.25 O sample in Fig. 26(f4), the tensile behavior of all the four alloys was isotropic. Among the designed alloys, 50Ti− 0.25 O exhibited one of the best combinations of ductility-strength, with the 1050 MPa ultimate tensile strength and 22% elongation.

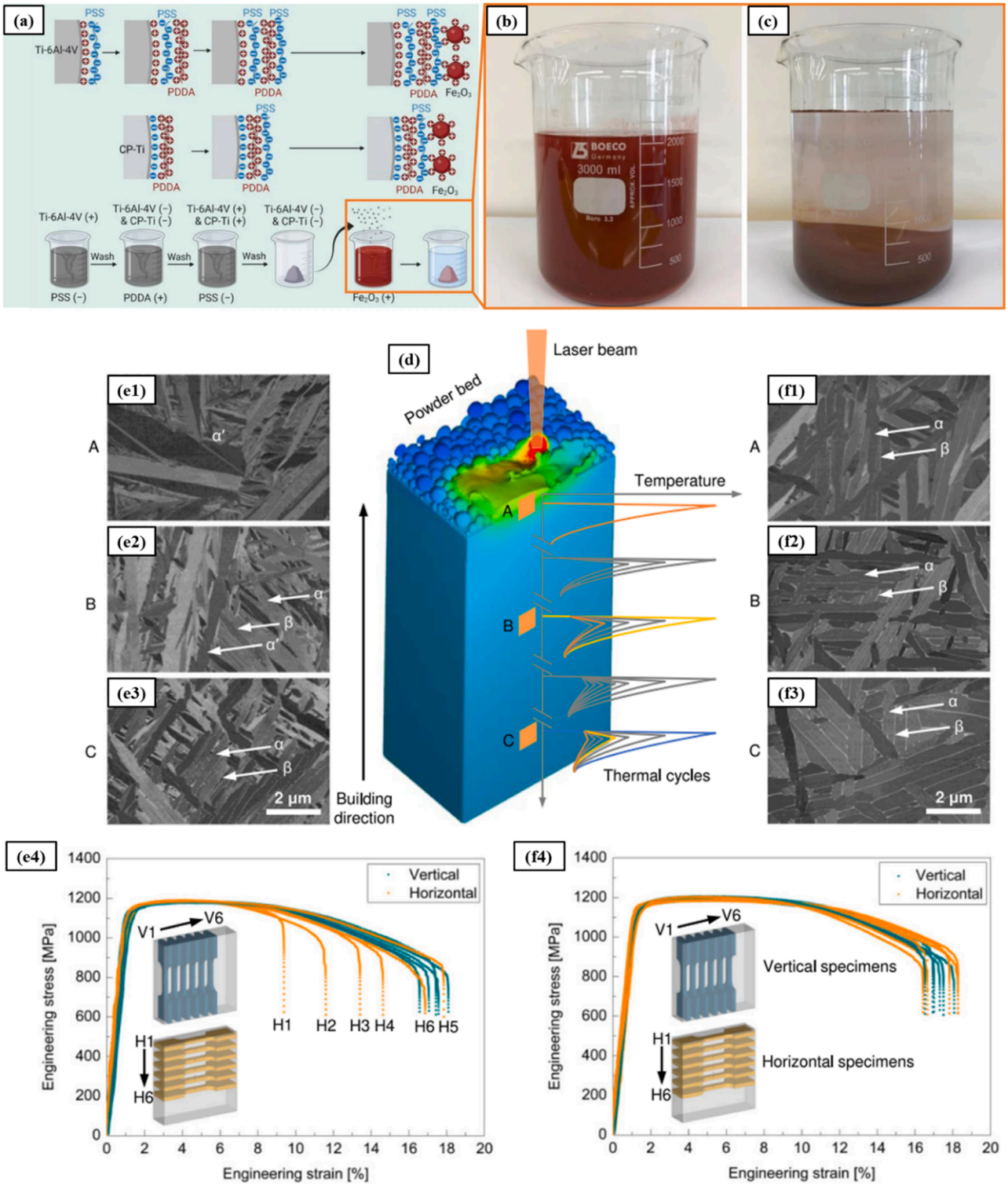

Fig. 26. (a-c) Feedstock preparation procedure for Ti-6Al-4V, CP-Ti, and Fe_2O_3 using the surface engineering methodology, (d) schematic of the SLM process along with thermal cycles in each layer, (e1-e3) SEM images of the microstructure of the SLM Ti-6Al-4V samples, (e4) stress-strain curves of horizontal and vertical SLM Ti-6Al-4 V tensile samples, (f1-f3) SEM images of the microstructure of the SLM 25Ti-0.25 O alloy (25 wt% CP-Ti and 0.25 wt% Fe_2O_3), (f4) horizontal and vertical stress-strain curves of SLM 25Ti-0.25 O samples.
Figure reproduced from [213].

4. Summary and perspectives

Fig. 27 illustrates the tensile properties of titanium alloy with different manufacturing methods. As shown in Fig. 27, UTS and elongation of the state-of-the-art AM such as in-situ heat treatment, high-intensity acoustic vibration, in-situ rolling, metallic and non-metallic alloying elements/nucleants, and deliberately introducing of LOF with subsequent HIP are comparable and in some cases even better than that of ASTM-approved cast and wrought Ti-6Al-4V alloy.

Generally, most of the introduced approaches in this paper add

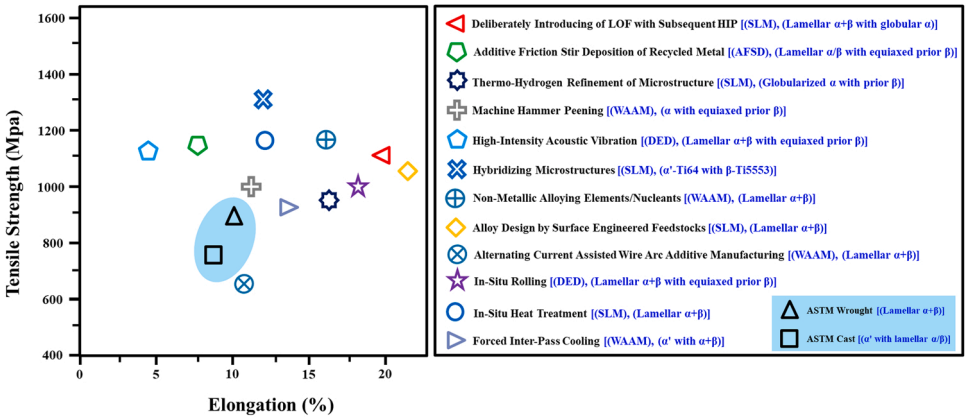

Fig. 27. Tensile strength and elongation of the introduced approaches vs. conventional ASTM cast and wrought methods [214] for titanium production.

additional processing steps that may increase manufacturing cost and time. Also, some cause changes in the chemical composition of the alloy which may be useful for mechanical performance, but detrimental for other properties such as corrosion and oxidation. Approaches that rely on mechanical deformation to drive recrystallization can preserve chemical composition, but they suffer from poor geometrical accuracy. Furthermore, the commercially available AM machines do not have most of the aforementioned capabilities introduced in this review paper to achieve the desired microstructures and mechanical properties. The following is a description of the challenges facing each new approach along with potential gaps that needs to be addressed:

- Despite recent progress in adding metallic, non-metallic, or ceramic nucleants/alloying elements to make printed Ti alloys with equiaxed grain structures, there are still many challenges that remain unresolved. One of these challenges is to find an effective nucleant element for each of the Ti alloys. Another challenge is to understand how the added nucleant will change the chemical composition of the respective Ti alloy and its properties. While most studies have focused on mechanical performance of these alloys, other properties such as corrosion and oxidation may be important for the intended use of the alloy.
- Applying a forced inter-pass cooling process can induce residual stress in the manufactured samples, which requires further post-processing treatments. Additionally, a systematic investigation of the different cooling gas flow rates and various cooling times and their effect on microstructure and properties should be considered.
- Using in-situ heat treatment, printed samples with engineered microstructures in each layer are attainable, which ultimately leads to the production of printed alloys with unique properties. However, if a single laser is used for both processing and heat treatment, it can result in longer manufacturing time. Use of multiple lasers or other heat sources is on the rise which can maintain the manufacturing time albeit the printers equipped with multiple lasers are going to be more expensive.
- In the MHP, due to small dimensions of the circular tracks created by the MHP, scaling up will be difficult as the processing time will become longer which impacts the manufacturing cost.
- One of the major issues in the development of hybridized microstructures is the alteration of the chemical composition of the Ti-6Al-4Vsamples. In addition, the microstructural heterogeneity may not be suitable for applications of these alloys under various loading and environmental conditions.
- For acoustic vibration, the effectiveness of this approach can be dropped for printing tall samples since the intensity of the acoustic vibration drops with distance from the source. In addition, this approach cannot be applied to all AM methods. For example, in the SLM methods, as the sample is made in a bed of powders, acoustic vibration cannot be used because vibration causes disturbance in the powder bed.
- For THRM, the existence of several initial heat treatment steps for inducing H_2 and then dehydrogenation for removing the induced hydrogen can increase energy, time, and final cost of printed parts. Additionally, one of the sensitive steps is adding and then removing hydrogen from the Ti-6Al-4V alloy. Based on the ASTM/ISO recommendations, the amount of maximum hydrogen in the Ti-6Al-4V samples should be lower than 0.01 wt%. Since controlling the amount of hydrogen and keeping it lower than the recommended value in ASTM/ISO standard is of great importance, the inducing hydrogen and then dehydrogenation steps would be challenging and requires tight control of the environment.
- For in-situ diode heating, use of additional heating source can enhance energy consumption and cost of manufactured products. In addition, as already mentioned, the machine that has been used in this method is a laboratory scale custom SLM machine and the effectiveness of this approach as well as its scalability needs further research.
- One of the strengths of in-situ rolling method is that it does not change the composition of the alloy to control the solidification process and microstructure. However, while in-situ rolling is a good fit for DED, it may not be a great option for PBF; if we use a small roller, it takes a long time to roll the whole powder bed and if we use a bigger roller, we will need much larger forces that will result in bulkier stages for PBF. Additionally, same as the many other state-of-the-art methods, the production time, energy consumption, and cost of the final products could increase.
- Samples produced with AFSD of recycled metals do not have melting/solidification-related problems such as defects, porosities, or columnar grains in the microstructures. However, some challenges are still present when using recycled metals from lath or milling machines. The remained metal chips can contain different kind of contaminations such as carbon, impurities, and oxides that could have a detrimental effect on mechanical properties of AFSDed samples.
- As mentioned earlier, deliberately introducing LOF with subsequent HIP is the latest proposed method for producing 3D printed Ti alloys with excellent mechanical performance. Given that the possibility of defects such as LOF in the microstructure of many printed parts seems inevitable, this method can be considered as an effective method to modify microstructure. Deliberately introducing LOF defects uses the defects in the microstructure as a strength and on the other hand, it does not change the chemical composition of the alloy. However, one challenge with this method is the possibility of geometrical changes during HIP process which affects the dimensional accuracy of printed parts.

- For alloy design by surface engineered feedstocks, the chemical coating and dissolution procedure can result in trapping of chemical residuals in the build which may have detrimental effect on mechanical properties or corrosion resistance. In addition, applying the surface engineering approach to prepare feedstock can be a disadvantage both from economical and time perspectives.

Like many manufacturing and post treatment processes, new methods that have been introduced in recent years to improve the microstructural and mechanical properties of 3D printed Ti alloys have their own advantages and challenges. However, the techniques presented here opened new avenues to control microstructure and properties of printed Ti alloys to achieve similar or even better properties than conventional manufacturing methods. By highlighting the existing challenges in this review paper and given the upward trend in the research for printing Ti alloys with excellent mechanical and microstructural performance, it is reasonable to expect that these challenges will be resolved in the near future.

CRediT authorship contribution statement

Atieh Moridi: Writing – review & editing, Supervision, Data curation, Conceptualization. **Frank Liou:** Writing – review & editing, Supervision. **Saeid Alipour:** Writing – review & editing, Writing – original draft, Data curation, Conceptualization. **Arezoo Emdadi:** Writing – review & editing, Supervision, Data curation, Conceptualization.

Declaration of Competing Interest

The authors declare that they have no known competing financial interests or personal relationships that could have appeared to influence the work reported in this paper.

Data Availability

No data was used for the research described in the article.

Acknowledgement

AM acknowledges financial support from National Science Foundation CAREER Award (CMMI-2046523), Office of Naval Research Young Investigator Award (N00014-22-1-2420), Department of Energy Early Career award (DE-SC0022860) and Johnson and Johnson WiSTEM2D Scholar's Award.

References

[1] Zhang, L.-C. and C. Yang, *Titanium alloys: formation, characteristics and industrial applications.* 2013.
[2] C. Veiga, J. Davim, A. Loureiro, Properties and applications of titanium alloys: a brief review, Rev. Adv. Mater. Sci. 32 (2) (2012) 133–148.
[3] A.M. Khorasani, et al., Titanium in biomedical applications—properties and fabrication: a review, J. Biomater. Tissue Eng. 5 (8) (2015) 593–619.
[4] A. Oryshchenko, et al., Marine titanium alloys: present and future, Inorg. Mater.: Appl. Res. 6 (6) (2015) 571–579.
[5] S.M. Javadhesari, S. Alipour, M. Akbarpour, Biocompatibility, osseointegration, antibacterial and mechanical properties of nanocrystalline Ti-Cu alloy as a new orthopedic material, Colloids Surf. B: Biointerfaces 189 (2020), 110889.
[6] F. Froes, Titanium: Physical Metallurgy, Processing, and Applications, ASM International, 2015.
[7] R.P. Kolli, A. Devaraj, A review of metastable beta titanium alloys, Metals 8 (7) (2018) 506.
[8] S.S. Sidhu, H. Singh, M.A.-H. Gepreel, A review on alloy design, biological response, and strengthening of β-titanium alloys as biomaterials, Mater. Sci. Eng.: C. 121 (2021), 111661.
[9] M. Sarraf, et al., A state-of-the-art review of the fabrication and characteristics of titanium and its alloys for biomedical applications, Bio Des. Manuf. (2021) 1–25.
[10] H. Fan, S. Yang, Effects of direct aging on near-alpha Ti–6Al–2Sn–4Zr–2Mo (Ti-6242) titanium alloy fabricated by selective laser melting (SLM), Mater. Sci. Eng.: A 788 (2020), 139533.
[11] A. Carrozza, et al., Towards customized heat treatments and mechanical properties in the SLM-processed Ti-6Al-2Sn-4Zr-6Mo alloy, Mater. Des. 215 (2022), 110512.
[12] S. Gialanella, A. Malandruccolo, Aerospace Alloys, Springer, 2020.
[13] H. Rosenberg, Titanium in the marine environment, in: OCEANS, 82, IEEE, 1982.
[14] L. Kunčická, R. Kocich, T.C. Lowe, Advances in metals and alloys for joint replacement, Prog. Mater. Sci. 88 (2017) 232–280.
[15] A. du Plessis, et al., Properties and applications of additively manufactured metallic cellular materials: a review, Prog. Mater. Sci. (2021), 100918.
[16] C. Leyens, M. Peters, Titanium and titanium alloys: fundamentals and applications, John Wiley & Sons, 2003.
[17] Takahashi, K., K. Mori, and H. Takebe. Application of titanium and its alloys for automobile parts. in MATEC Web of Conferences. 2020. EDP Sciences.
[18] H. Koizumi, et al., Application of titanium and titanium alloys to fixed dental prostheses, J. Prosthodont. Res. 63 (3) (2019) 266–270.
[19] M. Skilton, F. Hovsepian, The 4th industrial revolution, Springer, 2018.
[20] D.L. Bourell, T. Wohlers, Introduction to additive manufacturing, in: D.L. Bourell, et al. (Eds.), Additive Manufacturing Processes, ASM International, 2020, p. 0.
[21] M. Qian, D. Bourell, Additive manufacturing of titanium alloys, JOM 69 (12) (2017) 2677–2678.
[22] L.C. Zhang, et al., Additive manufacturing of titanium alloys. Encyclopedia of Materials: Metals and Alloys, Elsevier BV, 2021, pp. 256–274.
[23] Additive Manufacturing of Titanium Alloys, in Additive Manufacturing Processes, D.L. Bourell, et al., Editors. 2020, ASM International. p. 0.
[24] J.J. Lewandowski, M. Seifi, Metal additive manufacturing: a review of mechanical properties, Annu. Rev. Mater. Res. 46 (2016) 151–186.
[25] D.H. St John, et al., The challenges associated with the formation of equiaxed grains during additive manufacturing of titanium alloys. Key Engineering Materials, Trans Tech Publ., 2018.
[26] A.M. Beese, B.E. Carroll, Review of mechanical properties of Ti-6Al-4V made by laser-based additive manufacturing using powder feedstock, Jom 68 (3) (2016) 724–734.
[27] A. Moridi, et al., Deformation and failure mechanisms of Ti–6Al–4V as built by selective laser melting, Mater. Sci. Eng.: A 768 (2019), 138456.
[28] S. Sahoo, S. Roy, Additive manufacturing of titanium alloys: microstructure and texture evolution, defect formation and mechanical response. Additive Manufacturing, Elsevier, 2021, pp. 151–182.
[29] W. Hung, Post-Processing of Additively Manufactured Metal Parts, in: D. L. Bourell, et al. (Eds.), Additive Manufacturing Processes, ASM International, 2020, p. 0.
[30] A.H. Baker, P.C. Collins, J.C. Williams, New nomenclatures for heat treatments of additively manufactured titanium alloys, JOM 69 (7) (2017) 1221–1227.
[31] Z. Liu, et al., Effects of solution-aging treatments on microstructure features, mechanical properties and damage behaviors of additive manufactured Ti–6Al–4V alloy, Mater. Sci. Eng.: A 800 (2021), 140380.
[32] X.-Y. Zhang, et al., Effect of subtransus heat treatment on the microstructure and mechanical properties of additively manufactured Ti-6Al-4V alloy, J. Alloy. Compd. 735 (2018) 1562–1575.
[33] P. Chandramohan, et al., Laser additive manufactured Ti–6Al–4V alloy: heat treatment studies, Trans. Indian Inst. Met. 71 (3) (2018) 579–587.
[34] M. Gwak, et al., Post-annealing effect on the tensile deformation mechanism of a Ti–6Al–4V alloy manufactured via directed energy deposition, Mater. Sci. Eng.: A 836 (2022), 142729.
[35] X. Peng, et al., A review of post-processing technologies in additive manufacturing, J. Manuf. Mater. Process. 5 (2) (2021) 38.
[36] M. Seifi, et al., Overview of materials qualification needs for metal additive manufacturing, Jom 68 (3) (2016) 747–764.
[37] Agapovichev, A., et al. Possibilities and limitations of titanium alloy additive manufacturing. in MATEC Web of Conferences. 2018. EDP Sciences.
[38] S.C. Renjith, K. Park, G.E. Okudan Kremer, A design framework for additive manufacturing: integration of additive manufacturing capabilities in the early design process. Int. J. Precis. Eng. Manuf. 21 (2) (2020) 329–345.
[39] L.C. Campanelli, A review on the recent advances concerning the fatigue performance of titanium alloys for orthopedic applications, J. Mater. Res. 36 (1) (2021) 151–165.
[40] N. Sanaei, A. Fatemi, Defects in additive manufactured metals and their effect on fatigue performance: a state-of-the-art review, Prog. Mater. Sci. 117 (2021), 100724.
[41] F. Cao, et al., A review of the fatigue properties of additively manufactured Ti-6Al-4V, Jom 70 (3) (2018) 349–357.
[42] P. Li, et al., Critical assessment of the fatigue performance of additively manufactured Ti–6Al–4V and perspective for future research, Int. J. Fatigue 85 (2016) 130–143.
[43] A.H. Chern, et al., A review on the fatigue behavior of Ti-6Al-4V fabricated by electron beam melting additive manufacturing, Int. J. Fatigue 119 (2019) 173–184.
[44] A. Fatemi, et al., Fatigue behaviour of additive manufactured materials: an overview of some recent experimental studies on Ti-6Al-4V considering various processing and loading direction effects, Fatigue Fract. Eng. Mater. Struct. 42 (5) (2019) 991–1009.
[45] A. Gupta, C.J. Bennett, W. Sun, The role of defects and characterisation of tensile behaviour of EBM Additive manufactured Ti-6Al-4V: An experimental study at elevated temperature, Eng. Fail. Anal. 120 (2021), 105115.
[46] J. Pegues, et al., Fatigue of additive manufactured Ti-6Al-4V, part I: the effects of powder feedstock, manufacturing, and post-process conditions on the resulting microstructure and defects, Int. J. Fatigue 132 (2020), 105358.

[47] N. Kazantseva, et al., Martensitic transformations in Ti-6Al-4V (ELI) alloy manufactured by 3D Printing, Mater. Charact. 146 (2018) 101–112.
[48] M. Simonelli, Y.Y. Tse, C. Tuck, Effect of the build orientation on the mechanical properties and fracture modes of SLM Ti–6Al–4V, Mater. Sci. Eng.: A 616 (2014) 1–11.
[49] S. Pal, et al., Evolution of metallurgical properties of Ti-6Al-4V alloy fabricated in different energy densities in the Selective Laser Melting technique, J. Manuf. Process. 35 (2018) 538–546.
[50] D.K. Do, P. Li, The effect of laser energy input on the microstructure, physical and mechanical properties of Ti-6Al-4V alloys by selective laser melting, Virtual Phys. Prototyp. 11 (1) (2016) 41–47.
[51] H. Shipley, et al., Optimisation of process parameters to address fundamental challenges during selective laser melting of Ti-6Al-4V: a review, Int. J. Mach. Tools Manuf. 128 (2018) 1–20.
[52] Pegues, J., et al. Effect of process parameter variation on microstructure and mechanical properties of additively manufactured TI-6al-4v. in 2017 International Solid Freeform Fabrication Symposium. 2017. University of Texas at Austin.
[53] P. Nandwana, et al., Post-processing to modify the α phase micro-texture and β phase grain morphology in Ti-6Al-4V fabricated by powder bed electron beam melting, Metall. Mater. Trans. A 50 (7) (2019) 3429–3439.
[54] S. Gangireddy, E. Faierson, R. Mishra, Influences of post-processing, location, orientation, and induced porosity on the dynamic compression behavior of Ti–6Al–4V alloy built through additive manufacturing, J. Dyn. Behav. Mater. 4 (4) (2018) 441–451.
[55] Ó. Teixeira, et al., A review of heat treatments on improving the quality and residual stresses of the Ti–6Al–4V parts produced by additive manufacturing, Metals 10 (8) (2020) 1006.
[56] M. Ahlfors, Hot isostatic pressing for metal additive manufacturing, in: D. L. Bourell, et al. (Eds.), Additive Manufacturing Processes, ASM International, 2020, p. 0.
[57] Y. Xu, et al., Microstructure and corrosion behaviour of additively manufactured Ti–6Al–4V with various post-heat treatments, Mater. Sci. Technol. 35 (1) (2019) 89–97.
[58] J.R. Honnige, et al., Residual stress and texture control in Ti-6Al-4V wire+ arc additively manufactured intersections by stress relief and rolling, Mater. Des. 150 (2018) 193–205.
[59] S.L. Lu, et al., Microstructure and mechanical properties of long Ti-6Al-4V rods additively manufactured by selective electron beam melting out of a deep powder bed and the effect of subsequent hot isostatic pressing, Metall. Mater. Trans. A 46 (9) (2015) 3824–3834.
[60] M.-W. Wu, et al., Improved fatigue endurance ratio of additive manufactured Ti-6Al-4V lattice by hot isostatic pressing, Mater. Des. 134 (2017) 163–170.
[61] M. Muhammad, et al., Effect of heat treatments on microstructure/small-scale properties of additive manufactured Ti-6Al-4V, Int. J. Adv. Manuf. Technol. 103 (9) (2019) 4161–4172.
[62] M. Bermingham, et al., Optimising the mechanical properties of Ti-6Al-4V components produced by wire+ arc additive manufacturing with post-process heat treatments, J. Alloy. Compd. 753 (2018) 247–255.
[63] M. Kusano, et al., Tensile properties prediction by multiple linear regression analysis for selective laser melted and post heat-treated Ti-6Al-4V with microstructural quantification, Mater. Sci. Eng.: A 787 (2020), 139549.
[64] J. Hu, et al., Effect of heat treatment on microstructure and tensile properties of Ti-6Al-4V alloy produced by coaxial electron beam wire feeding additive manufacturing, JOM 73 (7) (2021) 2241–2249.
[65] Z. Liu, et al., A Review on Additive manufacturing of titanium alloys for aerospace applications: directed energy deposition and beyond Ti-6Al-4V, Jom 73 (6) (2021) 1804–1818.
[66] S. Wu, et al., Microstructural evolution and microhardness of a selective-laser-melted Ti–6Al–4V alloy after post heat treatments, J. Alloy. Compd. 672 (2016) 643–652.
[67] E. Sallica-Leva, et al., Ductility improvement due to martensite α′ decomposition in porous Ti–6Al–4V parts produced by selective laser melting for orthopedic implants, J. Mech. Behav. Biomed. Mater. 54 (2016) 149–158.
[68] E. Brandl, D. Greitemeier, Microstructure of additive layer manufactured Ti–6Al–4V after exceptional post heat treatments, Mater. Lett. 81 (2012) 84–87.
[69] A. Carrozza, et al., An investigation on the effect of different multi-step heat treatments on the microstructure, texture and mechanical properties of the DED-produced Ti-6Al-4 V alloy, Mater. Charact. (2022), 111958.
[70] C.V. Funch, et al., Targeted heat treatment of additively manufactured Ti-6Al-4V for controlled formation of Bi-lamellar microstructures, J. Mater. Sci. Technol. 81 (2021) 67–76.
[71] C.-L. Li, et al., Realizing superior ductility of selective laser melted Ti-6Al-4V through a multi-step heat treatment, Mater. Sci. Eng.: A 799 (2021), 140367.
[72] R. Sabban, et al., Globularization using heat treatment in additively manufactured Ti-6Al-4V for high strength and toughness, Acta Mater. 162 (2019) 239–254.
[73] Z. Zou, et al., Microstructure and tensile properties of additive manufactured Ti-6Al-4V with refined prior-β grain structure obtained by rapid heat treatment, Mater. Sci. Eng.: A 814 (2021), 141271.
[74] S. Gialanella, A. Malandruccolo, Titanium and titanium alloys. Aerospace Alloys, Springer International Publishing, Cham, 2020, pp. 129–189.
[75] M.-T. Tsai, et al., Heat-treatment effects on mechanical properties and microstructure evolution of Ti-6Al-4V alloy fabricated by laser powder bed fusion, J. Alloy. Compd. 816 (2020), 152615.
[76] T. Ahmed, H. Rack, Phase transformations during cooling in α+ β titanium alloys, Mater. Sci. Eng.: A 243 (1–2) (1998) 206–211.
[77] Villa, M., Metallurgical and mechanical modelling of Ti-6Al-4V for welding applications. 2016, University of Birmingham.
[78] R. Cottam, et al., Diffraction line profile analysis of 3D wedge samples of Ti-6Al-4V fabricated using four different additive manufacturing processes, Metals 9 (1) (2019) 60.
[79] S. Cao, et al., Role of martensite decomposition in tensile properties of selective laser melted Ti-6Al-4V, J. Alloy. Compd. 744 (2018) 357–363.
[80] H. Galarraga, et al., Effects of heat treatments on microstructure and properties of Ti-6Al-4V ELI alloy fabricated by electron beam melting (EBM), Mater. Sci. Eng.: A 685 (2017) 417–428.
[81] Z. Fan, H. Feng, Study on selective laser melting and heat treatment of Ti-6Al-4V alloy, Results Phys. 10 (2018) 660–664.
[82] Y. Zhai, H. Galarraga, D.A. Lados, Microstructure evolution, tensile properties, and fatigue damage mechanisms in Ti-6Al-4V alloys fabricated by two additive manufacturing techniques, Procedia Eng. 114 (2015) 658–666.
[83] B. Vrancken, et al., Heat treatment of Ti6Al4V produced by Selective Laser Melting: microstructure and mechanical properties, J. Alloy. Compd. 541 (2012) 177–185.
[84] H. Jaber, et al., Effects of annealing and solution treatments on the microstructure and mechanical properties of Ti6Al4V manufactured by Selective Laser Melting, Materials 15 (5) (2022) 1978.
[85] S. Raghavan, et al., Heat treatment of electron beam melted (EBM) Ti-6Al-4V: microstructure to mechanical property correlations, Rapid Prototyp. J. (2018).
[86] S.I. Shakil, et al., Post fabrication thermomechanical processing of additive manufactured metals: a review, J. Manuf. Process. 73 (2022) 757–790.
[87] A. Habibiyan, A.Z. Hanzaki, H.R. Abedi, An investigation into microstructure and high-temperature mechanical properties of selective laser-melted 316L stainless steel toward the development of hybrid Ampliforge process, Int. J. Adv. Manuf. Technol. 110 (1) (2020) 383–394.
[88] A. Mostafa, et al., Hot compression behavior and microstructure of selectively laser-melted IN718 alloy, Int. J. Adv. Manuf. Technol. 96 (1) (2018) 371–385.
[89] M. Bambach, et al., Hot workability and microstructure evolution of the nickel-based superalloy Inconel 718 produced by laser metal deposition, J. Alloy. Compd. 740 (2018) 278–287.
[90] A. Jedynak, et al., On the potential of using selective laser melting for the fast development of forging alloys at the example of waspaloy, Procedia Manuf. 47 (2020) 1149–1153.
[91] V. Popovich, et al., Creep and thermomechanical fatigue of functionally graded Inconel 718 produced by additive manufacturing. TMS annual meeting & exhibition, Springer,, 2018.
[92] Hirtler, M., et al. Investigation of microstructure and hardness of a rib geometry produced by metal forming and wire-arc additive manufacturing. in MATEC Web of Conferences. 2018. EDP Sciences.
[93] Y. Zhou, et al., Hot deformation induced microstructural evolution in local-heterogeneous wire+ arc additive manufactured 2219 Al alloy, J. Alloy. Compd. 865 (2021), 158949.
[94] X. You, et al., The precipitation behavior and hot deformation characteristics of electron beam smelted inconel 740 superalloy, J. Mater. Eng. Perform. 27 (4) (2018) 1580–1591.
[95] E. Roush, P. Kobryn, S. Semiatin, Anisotropy of plastic flow and microstructure evolution during hot working of laser-deposited Ti–6Al–4V, Scr. Mater. 45 (6) (2001) 717–724.
[96] I. Sizova, et al., Wire-arc additive manufacturing of pre-forms for forging of a Ti–6Al–4V turbine blade. AIP Conference Proceedings, AIP Publishing LLC,, 2019.
[97] P. Tao, et al., Microstructure, mechanical properties, and constitutive models for Ti–6Al–4V alloy fabricated by selective laser melting (SLM), Metals 9 (4) (2019) 447.
[98] M. Bambach, I. Sizova, A. Emdadi, Development of a processing route for Ti-6Al-4V forgings based on preforms made by selective laser melting, J. Manuf. Process. 37 (2019) 150–158.
[99] Y. Zhang, et al., Additive manufacturing of metallic materials: a review, J. Mater. Eng. Perform. 27 (1) (2018) 1–13.
[100] S. Semiatin, An overview of the thermomechanical processing of α/β titanium alloys: current status and future research opportunities, Metall. Mater. Trans. A 51 (6) (2020) 2593–2625.
[101] J. Williams, Thermo-mechanical processing of high-performance Ti alloys: recent progress and future needs, J. Mater. Process. Technol. 117 (3) (2001) 370–373.
[102] J.C. Williams, R.R. Boyer, Opportunities and issues in the application of titanium alloys for aerospace components, Metals 10 (6) (2020) 705.
[103] J.J. Burke, V. Weiss, Advances in deformation processing, Springer Science & Business Media, 2012.
[104] B. Verlinden, et al., Thermo-mechanical processing of metallic materials, Elsevier, 2007.
[105] A. Saboori, et al., Hot deformation behavior and flow stress modeling of Ti–6Al–4V alloy produced via electron beam melting additive manufacturing technology in single β-phase field, Mater. Sci. Eng.: A 792 (2020), 139822.
[106] M. Bambach, et al., Hybrid manufacturing of components from Ti-6Al-4V by metal forming and wire-arc additive manufacturing, J. Mater. Process. Technol. 282 (2020), 116689.
[107] M. Bambach, et al., On the hot deformation behavior of Ti-6Al-4V made by additive manufacturing, J. Mater. Process. Technol. 288 (2021), 116840.

[108] S. Hemes, et al., Microstructures and Mechanical Properties Of Hybrid, Additively Manufactured Ti6Al4V aftEr Thermomechanical Processing, Materials 14 (4) (2021) 1039.
[109] A. Maurya, et al., Optimization of hybrid manufacturing process combining forging and wire-arc additive manufactured Ti-6Al-4V through hot deformation characterization, J. Alloy. Compd. 894 (2022), 162453.
[110] A. Sombatmai, et al., Multiscale investigation of the influence of geometrical imperfections, porosity, and size-dependent features on mechanical behavior of additively manufactured Ti-6Al-4V lattice struts, Mater. Des. 209 (2021), 109985.
[111] V.-D. Le, et al., Fatigue behaviour of additively manufactured Ti-6Al-4V alloy: the role of defects on scatter and statistical size effect, Int. J. Fatigue 140 (2020), 105811.
[112] M.R. Kabir, H. Richter, Modeling of processing-induced pore morphology in an additively-manufactured Ti-6Al-4V alloy, Materials 10 (2) (2017) 145.
[113] F. Honarvar, A. Varvani-Farahani, A review of ultrasonic testing applications in additive manufacturinG: Defect evaluation, material characterization, and process control, Ultrasonics 108 (2020), 106227.
[114] C. Bellini, et al., Additive manufacturing processes for metals and effects of defects on mechanical strength: a review, Procedia Struct. Integr. 33 (2021) 498–508.
[115] A. Flodin, M. Andersson, A. Miedzinski, Full density powder metal components through Hot Isostatic Pressing, Met. Powder Rep. 72 (2) (2017) 107–110.
[116] J. Keist, S. Nayir, T. Palmer, Impact of hot isostatic pressing on the mechanical and microstructural properties of additively manufactured Ti–6Al–4V fabricated using directed energy deposition, Mater. Sci. Eng. A 787 (2020), 139454.
[117] J. Zhang, et al., Effect of multi-pass deformation on microstructure and flow behavior of Ti-6Al-4V alloy fabricated through hot isostatic pressing, Mater. Res. Express 8 (1) (2021), 016519.
[118] Liu, H., et al., Effect of Multi-Pass Deformation on Hot Flow Behavior and Spheroidization, Dynamic Recrystallization and Fusing Mechanism of Ti-6Al-4V Alloy Fabricated by Hot Isostatic Pressing. Dynamic Recrystallization and Fusing Mechanism of Ti-6Al-4V Alloy Fabricated by Hot Isostatic Pressing.
[119] J. Zhang, et al., Microstructure characterization of hot isostatic pressed Ti–6Al–4V alloy under uniaxial compression and post heat treatment, J. Mater. Res. Technol. 15 (2021) 7070–7084.
[120] S.K. Vajpai, et al., The development of high performance Ti-6Al-4V alloy via a unique microstructural design with bimodal grain size distribution, Metall. Mater. Trans. A 46 (2) (2015) 903–914.
[121] V.V. Popov, et al., Texturing and phase evolution in Ti-6Al-4V: Effect Of Electron beam melting process, powder re-using, and HIP treatment, Materials 14 (16) (2021) 4473.
[122] G. Kasperovich, J. Hausmann, Improvement of fatigue resistance and ductility of TiAl6V4 processed by selective laser melting, J. Mater. Process. Technol. 220 (2015) 202–214.
[123] E. Pessard, et al., High-cycle fatigue behavior of a laser powder bed fusion additive manufactured Ti-6Al-4V titanium: effect of pores and tested volume size, Int. J. Fatigue 149 (2021), 106206.
[124] A. Yadollahi, N. Shamsaei, Additive manufacturing of fatigue resistant materials: challenges and opportunities, Int. J. Fatigue 98 (2017) 14–31.
[125] T.P. Moran, et al., Hot isostatic pressing for fatigue critical additively manufactured Ti-6Al-4V, Materials 15 (6) (2022) 2051.
[126] R. Molaei, A. Fatemi, N. Phan, Significance of hot isostatic pressing (HIP) on multiaxial deformation and fatigue behaviors of additive manufactured Ti-6Al-4V including build orientation and surface roughness effects, Int. J. Fatigue 117 (2018) 352–370.
[127] R. Molaei, A. Fatemi, Crack paths in additive manufactured metallic materials subjected to multiaxial cyclic loads including surface roughness, HIP, and notch effects, Int. J. Fatigue 124 (2019) 558–570.
[128] P. Li, et al., Investigation of the mechanisms by which hot isostatic pressing improves the fatigue performance of powder bed fused Ti-6Al-4V, Int. J. Fatigue 120 (2019) 342–352.
[129] Zhang, B., et al. Effect of heat treatment and hot isostatic pressing on the morphology and size of pores in additive manufactured Ti-6Al-4V parts. in 2017 International Solid Freeform Fabrication Symposium. 2017. University of Texas at Austin.
[130] J. Wang, et al., Selective electron beam manufacturing of Ti-6Al-4V strips: effect of build orientation, columnar grain orientation, and hot isostatic pressing on tensile properties, JOM 70 (5) (2018) 638–643.
[131] P. Jamshidi, et al., Selective laser melting of Ti-6Al-4V: the impact of post-processing on the tensile, fatigue and biological properties for medical implant applications, Materials 13 (12) (2020) 2813.
[132] C. Liu, et al., Effect of hot isostatic pressing on microstructures and mechanical properties of Ti6Al4V fabricated by electron beam melting, Metals 10 (5) (2020) 593.
[133] A. Mahmud, et al., Mechanical behavior assessment of Ti-6Al-4V ELI alloy produced by laser powder bed fusion, Metals 11 (11) (2021) 1671.
[134] E. Tiferet, et al., Mapping the tray of electron beam melting of Ti-6Al-4V: properties and microstructure, Materials 12 (9) (2019) 1470.
[135] A. Mohammadhosseini, et al., Microstructure and mechanical properties of Ti–6Al–4V manufactured by electron beam melting process, Mater. Res. Innov. 17 (sup2) (2013) s106–s112.
[136] P. Barriobero-Vila, et al., Peritectic titanium alloys for 3D printing, Nat. Commun. 9 (1) (2018) 1–9.
[137] D. Zhang, et al., Additive manufacturing of ultrafine-grained high-strength titanium alloys, Nature 576 (7785) (2019) 91–95.
[138] B.A. Welk, et al., Use of alloying to effect an equiaxed microstructure in additive manufacturing and subsequent heat treatment of high-strength titanium alloys, Metall. Mater. Trans. A 52 (12) (2021) 5367–5380.
[139] Q. Chao, et al., Nanoparticle-mediated ultra grain refinement and reinforcement in additively manufactured titanium alloys, Addit. Manuf. 46 (2021), 102173.
[140] P. Huo, et al., Deformation strengthening mechanism of in situ TiC/TC4 alloy nanocomposites produced by selective laser melting, Compos. Part B: Eng. 225 (2021), 109305.
[141] W.H. Yu, et al., Particle-reinforced metal matrix nanocomposites fabricated by selective laser melting: a state of the art review, Prog. Mater. Sci. 104 (2019) 330–379.
[142] M. Bermingham, et al., Controlling the microstructure and properties of wire arc additive manufactured Ti–6Al–4V with trace boron additions, Acta Mater. 91 (2015) 289–303.
[143] R. Chen, et al., Modification of α-phase of wire+ arc additive manufactured Ti-6Al-4 V alloy with boron addition, Mater. Charact. 169 (2020), 110616.
[144] E. Fereiduni, A. Ghasemi, M. Elbestawi, Unique opportunities for microstructure engineering via trace B4C addition to Ti-6Al-4V through laser powder bed fusion process: As-built and heat-treated scenarios, Addit. Manuf. 50 (2022), 102557.
[145] X. Wang, et al., Hierarchical grain refinement during the laser additive manufacturing of Ti-6Al-4V alloys by the addition of micron-sized refractory particles, Addit. Manuf. 45 (2021), 102045.
[146] L. Liu, et al., In-situ nitrogen strengthening of selective laser melted Ti6Al4V with superior mechanical performance, Addit. Manuf. 46 (2021), 102142.
[147] C. Chen, et al., Microstructure evolution and mechanical properties of laser additive manufactured Ti6Al4V alloy under nitrogen-argon reactive atmosphere, Mater. Sci. Eng.: A 841 (2022), 143076.
[148] W. Wei, et al., In-situ laser additive manufacturing of Ti6Al4V matrix composites by gas–liquid reaction in dilute nitrogen gas atmospheres, Mater. Des. 202 (2021), 109578.
[149] L. Zhu, et al., Ti6Al4V matrix composites fabricated by laser powder bed fusion in dilute nitrogen, Mater. Sci. Technol. 38 (4) (2022) 207–214.
[150] P. Morton, et al., In situ selective laser gas nitriding for composite TiN/Ti-6Al-4V fabrication via laser powder bed fusion, J. Mater. Sci. Technol. 45 (2020) 98–107.
[151] A. Issariyapat, et al., Refined grain formation behavior and strengthening mechanism of α-titanium with nitrogen fabricated by selective laser melting, Addit. Manuf. 36 (2020), 101537.
[152] A. Issariyapat, et al., Strengthening and deformation mechanism of selective laser-melted high-concentration nitrogen solute α-Ti materials with heterogeneous microstructures via heat treatment, Mater. Sci. Eng. A 826 (2021), 141935.
[153] K. Kondoh, et al., Selective laser-melted titanium materials with nitrogen solid solutions for balanced strength and ductility, Mater. Sci. Eng.: A 790 (2020), 139641.
[154] B. Wu, et al., The effects of forced interpass cooling on the material properties of wire arc additively manufactured Ti6Al4V alloy, J. Mater. Process. Technol. 258 (2018) 97–105.
[155] W. Xu, et al., Additive manufacturing of strong and ductile Ti–6Al–4V by selective laser melting via in situ martensite decomposition, Acta Mater. 85 (2015) 74–84.
[156] W. Xu, et al., In situ tailoring microstructure in additively manufactured Ti-6Al-4V for superior mechanical performance, Acta Mater. 125 (2017) 390–400.
[157] A. Zafari, M. Barati, K. Xia, Controlling martensitic decomposition during selective laser melting to achieve best ductility in high strength Ti-6Al-4V, Mater. Sci. Eng.: A 744 (2019) 445–455.
[158] M. Motyka, Martensite formation and decomposition during traditional and AM processing of two-phase titanium alloys—An overview, Metals 11 (3) (2021) 481.
[159] X. Chen, C. Qiu, In-situ development of a sandwich microstructure with enhanced ductility by laser reheating of a laser melted titanium alloy, Sci. Rep. 10 (1) (2020) 1–12.
[160] J. Lv, et al., Achieving high strength and ductility in selective laser melting Ti-6Al-4V alloy by laser shock peening, J. Alloy. Compd. (2021), 163335.
[161] Kalentics, N., R. Logé, and E. Boillat, Method and device for implementing laser shock peening or warm laser shock peening during selective laser melting. 2020, Google Patents.
[162] Kalentics, N. and R. Logé, Laser treatment systems and methods for in-situ laser shock peening (lsp) treatment of parts during production thereof by a selective laser sintering or melting (sls/slm) process, and additive manufacturing systems and methods implementing the same. 2021.
[163] N. Kalentics, et al., 3D laser shock peening as a way to improve geometrical accuracy in selective laser melting, Int. J. Adv. Manuf. Technol. 101 (5) (2019) 1247–1254.
[164] Neto, L., et al. Mechanical properties enhancement of additive manufactured Ti-6Al-4V by machine hammer peening. in International Conference on Advanced Surface Enhancement. 2019. Springer.
[165] J. Hönnige, et al., The effectiveness of grain refinement by machine hammer peening in high deposition rate wire-arc AM Ti-6Al-4V, Metall. Mater. Trans. A 51 (7) (2020) 3692–3703.
[166] A. Zafari, K. Xia, Superior titanium from hybridised microstructures–a new strategy for future alloys, Scr. Mater. 173 (2019) 61–65.
[167] C. Todaro, et al., Grain structure control during metal 3D printing by high-intensity ultrasound, Nat. Commun. 11 (1) (2020) 1–9.
[168] Y. Cui, C. Xu, Q. Han, Microstructure improvement in weld metal using ultrasonic vibrations, Adv. Eng. Mater. 9 (3) (2007) 161–163.
[169] T. Yuan, S. Kou, Z. Luo, Grain refining by ultrasonic stirring of the weld pool, Acta Mater. 106 (2016) 144–154.
[170] A. Ramirez, et al., Potency of high-intensity ultrasonic treatment for grain refinement of magnesium alloys, Scr. Mater. 59 (1) (2008) 19–22.

[171] T. Atamanenko, et al., Criteria of grain refinement induced by ultrasonic melt treatment of aluminum alloys containing Zr and Ti, Metall. Mater. Trans. A 41 (8) (2010) 2056–2066.
[172] M. Knezevic, et al., Thermo-hydrogen refinement of microstructure to improve mechanical properties of Ti–6Al–4V fabricated via laser powder bed fusion, Mater. Sci. Eng.: A 809 (2021), 140980.
[173] W.L. Smith, Effects of in situ Surface Layer Heating on Laser Powder Bed Fusion of 316L Stainless Steel, University of California, Davis, 2021.
[174] J.D. Roehling, et al., Reducing residual stress by selective large-area diode surface heating during laser powder bed fusion additive manufacturing, Addit. Manuf. 28 (2019) 228–235.
[175] X. Tian, et al., Isotropic and improved tensile properties of Ti-6Al-4V achieved by in-situ rolling in direct energy deposition, Addit. Manuf. 46 (2021), 102151.
[176] K. Cheng, et al., Additive manufacturing of Ti-6Al-4V alloy by hybrid plasma-arc deposition and microrolling: grain morphology, microstructure, and tensile properties, Sci. China Technol. Sci. (2022) 1–9.
[177] P.A. Colegrove, et al., High pressure interpass rolling of wire+ arc additively manufactured titanium components. Advanced Materials Research, Trans Tech Publ, 2014.
[178] Szost, B., et al. High pressure interpass rolling of Wire+ Arc Additvely Manufactured titanium components. in ECRS-9: European Conference on Residual Stresses. 2014.
[179] F. Martina, et al., Microstructure of interpass rolled wire+ arc additive manufacturing Ti-6Al-4V components, Metall. Mater. Trans. A 46 (12) (2015) 6103–6118.
[180] J. Donoghue, et al., The effectiveness of combining rolling deformation with Wire–Arc Additive Manufacture on β-grain refinement and texture modification in Ti–6Al–4V, Mater. Charact. 114 (2016) 103–114.
[181] J. Hönnige, et al., Residual stress and texture control in Ti-6Al-4V wire+ arc additively manufactured intersections by stress relief and rolling, Mater. Des. 150 (2018) 193–205.
[182] F. Martina, et al., Residual stress of as-deposited and rolled wire+ arc additive manufacturing Ti–6Al–4V components, Mater. Sci. Technol. 32 (14) (2016) 1439–1448.
[183] J. Donoghue, et al., On the observation of annealing twins during simulating β-grain refinement in Ti–6Al–4V high deposition rate AM with in-process deformation, Acta Mater. 186 (2020) 229–241.
[184] H. Zhang, et al., Comparison of energy consumption between hybrid deposition & micro-rolling and conventional approach for wrought parts, J. Clean. Prod. 279 (2021), 123307.
[185] Z.Y. Hang, et al., Non-beam-based metal additive manufacturing enabled by additive friction stir deposition, Scr. Mater. 153 (2018) 122–130.
[186] E. Farabi, et al., Microstructure and mechanical properties of Ti6Al4V alloys fabricated by additive friction stir deposition, Addit. Manuf. Lett. 2 (2022), 100034.
[187] F. Khodabakhshi, A. Gerlich, Potentials and strategies of solid-state additive friction-stir manufacturing technology: A critical review, J. Manuf. Process. 36 (2018) 77–92.
[188] A.K. Srivastava, N. Kumar, A.R. Dixit, Friction stir additive manufacturing–an innovative tool to enhance mechanical and microstructural properties, Mater. Sci. Eng.: B 263 (2021), 114832.
[189] N. Tuncer, A. Bose, Solid-state metal additive manufacturing: a review, JOM 72 (9) (2020) 3090–3111.
[190] H.Z. Yu, R.S. Mishra, Additive friction stir deposition: a deformation processing route to metal additive manufacturing, Mater. Res. Lett. 9 (2) (2021) 71–83.
[191] S. Rathee, et al., Metal additive manufacturing using friction stir engineering: A review on microstructural evolution, tooling and design strategies, CIRP J. Manuf. Sci. Technol. 35 (2021) 560–588.
[192] R.S. Mishra, Z. Ma, Friction stir welding and processing, Mater. Sci. Eng. R: Rep. 50 (1–2) (2005) 1–78.
[193] D. Lohwasser, Z. Chen, Friction stir welding: From basics to applications, Elsevier, 2009.
[194] M.K. Besharati-Givi, P. Asadi, Advances in friction-stir welding and processing, Elsevier, 2014.
[195] Y. Zhang, et al., Review of tools for friction stir welding and processing, Can. Metall. Q. 51 (3) (2012) 250–261.
[196] L. Cui, et al., Recent progress in friction stir welding tools used for steels, J. Iron Steel Res. Int. 25 (5) (2018) 477–486.
[197] R. Rai, et al., friction stir welding tools, Sci. Technol. Weld. Join. 16 (4) (2011) 325–342.
[198] A. Heidarzadeh, et al., Friction stir welding/processing of metals and alloys: a comprehensive review on microstructural evolution, Prog. Mater. Sci. 117 (2021), 100752.
[199] Swarnkar, A., et al. A review on Friction Stir Welding: An environment friendly welding technique. in 2016 IEEE Region 10 Humanitarian Technology Conference (R10-HTC). 2016. IEEE.
[200] P. Agrawal, et al., Processing-structure-property correlation in additive friction stir deposited Ti-6Al-4V alloy from recycled metal chips, Addit. Manuf. 47 (2021), 102259.
[201] Kim, F.H., F.H. Kim, and S.P. Moylan, Literature review of metal additive manufacturing defects. 2018: US Department of Commerce, National Institute of Standards and Technology ….
[202] N. Sanaei, A. Fatemi, N. Phan, Defect characteristics and analysis of their variability in metal L-SLMadditive manufacturing, Mater. Des. 182 (2019), 108091.
[203] T. Mukherjee, T. DebRoy, Mitigation of lack of fusion defects in powder bed fusion additive manufacturing, J. Manuf. Process. 36 (2018) 442–449.
[204] Brennan, M., J.S. Keist, and T.A. Palmer, Defects in Metal Additive Manufacturing Processes, in Additive Manufacturing Processes, D.L. Bourell, et al., Editors. 2020, ASM International. p. 0.
[205] H. Gong, et al., Analysis of defect generation in Ti–6Al–4V parts made using powder bed fusion additive manufacturing processes, Addit. Manuf. 1 (2014) 87–98.
[206] H. Masuo, et al., Influence of defects, surface roughness and HIP on the fatigue strength of Ti-6Al-4V manufactured by additive manufacturing, Int. J. Fatigue 117 (2018) 163–179.
[207] E. Wycisk, et al., Effects of defects in laser additive manufactured Ti-6Al-4V on fatigue properties, Phys. Procedia 56 (2014) 371–378.
[208] J. Yu, et al., Detection of internal holes in additive manufactured Ti-6Al-4V part using laser ultrasonic testing, Appl. Sci. 10 (1) (2020) 365.
[209] J. Bustillos, J. Kim, A. Moridi, Exploiting lack of fusion defects for microstructural engineering in additive manufacturing, Addit. Manuf. 48 (2021), 102399.
[210] A. Moridi, et al., Solid-state additive manufacturing of porous Ti-6Al-4V by supersonic impact. Appl. Mater. Today 21 (2020), 100865.
[211] A. Moridi, et al., Cold spray coating: review of material systems and future perspectives, Surf. Eng. 30 (6) (2014) 369–395.
[212] J. Huang, et al., Microstructure regulation of titanium alloy functionally gradient materials fabricated by alternating current assisted wire arc additive manufacturing, Mater. Des. 218 (2022), 110731.
[213] J. Zhang, et al., Designing against phase and property heterogeneities in additively manufactured titanium alloys, Nat. Commun. 13 (1) (2022) 1–10.
[214] D. Zhang, et al., Metal alloys for fusion-based additive manufacturing, Adv. Eng. Mater. 20 (5) (2018), 1700952.